

DTIC FILE COPY

GA-C19465
(3/89)

(2)

HIGH-TEMPERATURE CERAMIC SUPERCONDUCTORS

For Period
January 1, - March 31, 1989

April 10, 1989

Prepared for:

OFFICE OF NAVAL RESEARCH
800 North Quincy Street
Arlington, Virginia 22217-5000

DTIC
ELECTE
MAY 0 1 1989
S D D

AD-A207 333

DARPA/ONR Contract N00014-88-C-0714

GA Project 3850

Prepared by:

- K. S. Mazdiasni, Program Manager
- K. C. Chen
- W. J. DeHope
- Y. R. Lin-Liu
- B. W. McQuillan
- F. C. Montgomery
- R. B. Stephens

DISTRIBUTION STATEMENT A
Approved for public release;
Distribution Unlimited

Approved by: *T. D. Gulden*
T. D. Gulden
Director, Defense Materials

The views and conclusions contained in this quarterly report are those of the authors and should not be interpreted as necessarily representing the official policies, either expressed or implied, of the Defense Advanced Research Projects Agency or the U. S. Government.



0 8 9 5 0 1 1 0 4

CONTENTS

1.	INTRODUCTION	1-1
1.1.	Project Outline	1-1
2.	PROGRESS	2-1
2.1.	Task 1 - Metal Alkoxide Synthesis and Processing	2-1
2.1.1.	Synthesis	2-1
2.1.2.	Experimental	2-3
2.1.3.	Choice of Electrolytes	2-4
2.1.4.	Choice of Electrodes and Switching Electrodes	2-5
2.1.5.	Characterization of Green-Black Product	2-6
2.1.6.	Electrolysis in Ethoxyethanol	2-8
2.2.	Metal Alkoxides Precursor Compounds.	2-8
2.2.1.	Synthesis	2-8
2.2.2.	Experimental	2-10
2.2.3.	Results and Discussion	2-11
3.	FIBER HEAT TREATMENT	3-1
3.1.	Optimization of Fiber Heat Treatment Schedule	3-1
3.2.	Continuous Fiber Drawing Development	3-9
3.3.	Fiber Preferred Crystallographic-Orientation Development (Texturing)	3-9
3.4.	Thin Film Preparation	3-18
4.	TECHNIQUE FOR MEASURING 123 RESISTIVITY AS A FUNCTION OF TEMPERATURE AT MICROWAVE FREQUENCIES	4-1
5.	THE EFFECT OF FLUX CREEP ON THE SURFACE RESISTANCE OF HIGH T_c SUPERCONDUCTORS	5-1
5.1.	Introduction	5-1
5.2.	Flux Creep Equations	5-1
5.3.	Superconducting Resistance - Zero Frequency	5-6
5.4.	Superconducting Resistance - High Frequency	5-9
5.4.1.	High Q Cavities	5-12
5.5.	Summary	5-14

6. REFERENCES	6-1
APPENDIX A	A-1

FIGURES

2-1. Comparison of thermal decomposition of 123 precursor powders produced with additives during the hydrolysis step	2-15
2-2. Thermal decomposition of powders produced by hydrolyzing Y/Ba alkoxide and Cu(II) compound in presence of H ₂ O ₂	2-16
2-3. Weight loss during ramp and hold test of 123 precursor powder prepared using H ₂ O ₂ additive	2-17
2-4. SEM photographs of film produced by dip coating and rapid drying at 130° and 170°C	2-19
3-1. Isothermal TGA on preceramic fiber (0.5 to 1 mm diameter) with 2 h at each temperature	3-2
3-2. Isothermal TGA curve of preceramic fiber for 5 h hold at 200° and 250°C and 2 h hold at 300°C and above	3-3
3-3. X-ray diffraction of fiber calcined at 750°C for (a) 1 h; (b) 2 h; and (c) 4 h	3-5
3-4. X-ray diffraction of fiber calcined at 800°C for (a) 1 h; (b) 4 h	3-6
3-5. X-ray diffraction of fiber heat-treated at (a) 850°C for 4 h and (b) 900°C for 4 h	3-7
3-6. Time-temperature-phase diagram for the formation of YBa ₂ Cu ₃ O _{7-x} phase	3-8
3-7. SEM micrograph of YBa ₂ Cu ₃ O _{7-x} fiber with stepwise annealing below 450°C and maximum calcining temperature of 900°C, 3 h showing more uniform density distribution in the cross section	3-10
3-8. SEM micrograph of YBa ₂ Cu ₃ O _{7-x} fiber calcined stepwise below 450°C and with maximum annealing temperature of 970°C, 2 h showing excess grain growth	3-11
3-9(a). Continuous preceramic fibers mechanical drawn (up-drawing method) from the polymeric solution	3-12
3-9(b). Continuous preceramic fiber spool prepared by the up-drawing method	3-12
3-10. Continuous preceramic fiber prepared by the down-drawing and extrusion method	3-13

FIGURES (Continued)

3-11. (a) DyBa₂Cu₃O_{7-x} powder prepared by the pyrolysis of solution coated on paper filaments and (b) a higher magnification shows the crystals are loosely agglomerated even after 900°C 4 h heat treatment 3-15

3-12. DyBa₂Cu₃O_{7-x} powder calcined at (a) 900°C, 4 h and (b) 900°C, 8 h 3-16

3-13. X-ray diffraction of DyBa₂Cu₃O_{7-x} powder calcined at 800°C, 16 h 3-17

3-14. X-ray diffraction of YBa₂Cu₃O_{7-x} film on YSZ substrates 3-19

5-1. Effect of Lorentz force $J \times B$ on the energy barrier to a unit length of flux bundle in a pinning site 5-4

5-2. Effective resistivity from flux creep for a high T_c superconductor with $T_c = 92$ K, $\xi_{\perp} = 2.5$ nm, $\xi_{\parallel} = 0.5$ nm, and $H_c = 0.82$ T (this gives $U_0 \approx 0.05$ eV), and $d_{pin} = 1.5$ nm 5-8

5-3. When flux lines are floppy, the Lorentz force bows them out between pinning sites 5-11

TABLES

2-1. Chemical analysis of copper isopropoxide 2-7

2-2. Chemical analysis of copper alkoxide in ethoxyethanol 2-9

2-3. Molar ratio of additives used during hydrolysis and polycondensation of alkoxides 2-12

2-4. Stability and products of hydrolyzing solutions of 123 alkoxides with additives 2-13

5-1. Material parameters 5-15

DTIC
COPY
INSPECTOR
6

SEARCHED	INDEXED
SERIALIZED	FILED
<p><i>see previous</i> <i>rpts. 1+2</i></p>	
<p>DTIC</p>	
<p>A-1</p>	

1. INTRODUCTION

This is the third quarterly progress report on the work performed in the period from January 1, 1989 through March 31, 1989 on Office of Naval Research (ONR) Contract N00014-88-C-0714, entitled "High-Temperature Ceramic Superconductors." The principal objectives of this program are (1) to demonstrate fabrication of high-temperature ceramic superconductors that can operate at or above 90 K with appropriate current density, J_c , in forms useful for application in resonant cavities, magnets, motors, sensors, computers, and other devices; and (2) to fabricate and demonstrate selected components made of these materials, including microwave cavities and magnetic shields. (mgj)

1.1. PROJECT OUTLINE

This program has been divided into six tasks: (1) metal alkoxide synthesis and processing, (2) microstructural evaluation and property measurement, (3) electrical and magnetic property measurement, (4) superconductor ceramic processing, (5) component fabrication and demonstration, and (6) reporting.

Task 1 is to synthesize a homogeneous alkoxide solution that contains all the constituent elements which can be easily made to powders, thin film, or drawn into fiber form. Ideally, this solution should possess precise stoichiometry, adequate stability, polymerizability, adherence, and spinnability. Also, the polymeric materials formed from this solution should be thermosetting, be able to be dissolved in organic solvents and contain as little as possible low-temperature pyrolyzable organics with high char yield.

Task 2 is to study the microstructure as a function of processing parameters. The study includes: density, pore size and pore size distribution, phase identification, chemical composition and purity, environmental stability, effects of heat treatment, residual strain, seeding, annealing in magnetic fields, and epitaxy on grain growth and orientation.

Task 3 is to study the electrical and magnetic properties of the $\text{YBa}_2\text{Cu}_3\text{O}_7$ (123) high T_c ceramic superconductors. It will include both the ac electrical resistance (R_{ac}) and the ac magnetic susceptibility (χ_{ac}).

Task 4 is an investigation of superconductor ceramic processing. Most of the important applications of superconductors require material in the form of fiber or films. Magnets, conductors, motors, and generators are examples of applications employing fiber; while detectors, microwave cavities, and microcircuitry require superconducting material in the form of films. The sol-gel process is ideally suited to producing materials in these forms; in fact, it is used commercially to produce antireflection and mirror coatings, and to produce continuous ceramic fibers, for structural reinforcement in composite materials, and for thermal insulation.

Task 5 is to demonstrate component fabrication. General Atomics (GA) will design and build a high Q, high T_c superconducting cavity using its unique sol-gel coating process capabilities. This task would proceed after some initial coating tests verified dc superconductivity and questions of adhesiveness, surface preparation, and processing procedures are answered. As the fabrication process and the materials quality are improved throughout the three-year program, two additional cavities will be constructed and tested. Coupling would be through a waveguide inductive iris into an end wall with a logarithmic decrement technique of Q measurement being considered most appropriate for the

high Q anticipated. An X-band (10 GHz) frequency choice allows for convenient dimensions of 4.3 cm diameter by 2.8 cm height.

This report will focus mostly on Tasks 1, 2, 4, and 5.

2. PROGRESS

2.1. TASK 1 - METAL ALKOXIDE SYNTHESIS AND PROCESSING

2.1.1. Synthesis

In the synthesis of $\text{YBa}_2\text{Cu}_3\text{O}_7$ via the alkoxide sol-gel route, the yttrium and barium alkoxides can be easily made in high purity by direct reaction of the metals with anhydrous alcohols. However, the synthesis of copper alkoxides cannot be performed by the direct reaction of copper metals with alcohol. In previous reports, we discussed the reaction



where M is an alkali metal and X is halide. When X is fluoride, and M is Li or Na, one observes Cu(iPrO)_2 with some 300 to 1000 ppm of MX, after copious washing. Commercial samples of $\text{Cu(OCH}_3)_2$ showed high chloride content, which can be lowered by washing. These levels of contamination sent us looking for alternative syntheses where the copper alkoxide could be obtained in a higher purity, while still obtaining reasonable multigram quantities.

Copper metal does not rapidly react with alcohol, to make copper alkoxide, because copper is not sufficiently electropositive. One way to increase copper's electropositivity is to impose a voltage on copper, in an electrochemical cell, so as to force the desired oxidation-reduction:



Copper would be oxidized at the anode, and hydrogen would be evolved at the cathode. Cu(OR)_2 would be formed in a reaction formally identical to the reactions of Y and Ba. Such a reaction was reported by Banait and Pahil (Ref. 1) using a dimethyl formamide (DMF) solution. In this reaction yields of greater than 80% were claimed.

While the above reaction appears simple and straightforward, other complications may occur, which would reduce the overall yield and purity of the copper alkoxide:

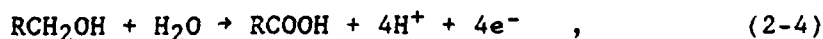
1. For this synthesis, electrolyte salts are added to the solution to increase the conductivity. Such ions may react with the principle product. For instance, quaternary ammonium salts $\text{R}_4\text{N}^+\text{Cl}^-$ might be used:
 - a. Cl^- may be oxidized to Cl_2 . This is unlikely in this system.
 - b. Formation of Cu(OR)Cl or CuCl_2 may occur, especially in the initial minutes when the concentration of chloride exceeds that of copper or alkoxide.

The above reactions would remove electrolyte, so the solution grows more resistive until no current passes.

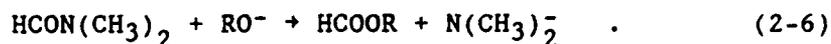
Our initial work used $\text{R}_4\text{N}^+\text{Cl}^-$, but other electrolytes were later used (PF_6^- , BF_4^-) which ought not to react with Cu(OR)_2 .

2. Other reactions might occur as side reactions, depending on the applied voltage, presence of other species such as water, and possible reactions of the solvent:

a. Oxidation of the solvent is possible, especially if the applied voltage is greater than ~3 to 5 V. For instance,



b. DMF is used as a solvent, and alkoxide is a strong base, so the following reaction is possible:



There are few ways to limit the occurrence of many of these side reactions.

2.1.2. Experimental

In general, a three neck flask, 250 to 500 ml, was filled with freshly distilled anhydrous alcohol. (In some initial work, DMF was a solvent.) Electrolyte was necessary, as the alcohol itself was very resistive. Sufficient electrolyte was added, so that if the electrolyte was consumed, all electrolyte would be used up after the passage of 10 to 15 coulombs. (This coulomb quantity corresponds to an electrolyte molarity of 0.1 to 1.0 mM.) Two copper rod electrodes (oxygen free) were inserted through one neck, a bubbler was added to a second neck, and N₂ as bubbled for 5 to 10 min through the stirred solution. The bubbling was stopped, the third neck capped, and the electrolysis was begun.

The electrolysis was done under constant current conditions, with a current generally selected at 50 mA if possible. The EG&G potentiostat would apply voltage, up to 100 V, across the electrodes, in order to obtain and maintain a 50 mA current. Such a current would produce 4.0 g cupric isopropoxide in 24 h, while the electrolyte would be consumed in 5 to 10 min. Since the infrared (IR) drop across the electrodes would rise the total voltage required, the electrodes were placed ~3 to 5 mm apart, to minimize the IR drop.

2.1.3. Choice of Electrolytes

In t-butanol, the electrolytes KBF_4 , NH_4Cl , Me_4NCl , and $\phi_4\text{PCl}$ all increased the conductivity to some degree. However, there were not dramatic increases in conductivity, so the work shifted to isopropanol.

In early work, isopropanol was used in DMF, with Me_4NCl . The tetramethyl ammonium chloride did not initially dissolve entirely. However, as the electrolysis proceeded, the undissolved salt did dissolve. This dissolution implied either the electrolyte was oxidized/reduced, or the electrolyte was reacting with the oxidation-reduction products. The latter possibility was more likely, since there was a visual absence of Cl_2 evolution, and the overload appeared once all the solid had disappeared. A coating appeared on the copper anode. Upon reversing the current flow, more current could flow. The electrolyte had not been destroyed, but reduction of the surface coating reintroduced the electrolyte into the solution. Two clues came from this study. First, one might suspect that chloride is too nucleophilic, and will not remain an inert electrolyte. Second, resistive coatings on the electrodes, which plagued the early work, could be removed or diminished by reversing the electrode polarity.

At this point, tetrabutyl ammonium-tetrafluoroborate (TBA-BF_4) was tried as an electrolyte. It dissolved readily, and the BF_4 ion is much less nucleophilic. We observed significantly higher total coulombs

10 to 100 times the coulombs required to consume the electrolyte. TBA-BF₄ was used in all further experiments.

Other electrolytes were tried in isopropanol. TBA-tetraphenyl borate was insoluble, as was TBA-hexafluoro phosphate. Barium metal was put into isopropanol, to make barium isopropoxide. This salt would make an ideal electrolyte, since a stoichiometric Ba:Cu ratio could be obtained in one synthesis. However, while the barium isopropoxide was soluble, it did not behave as an electrolyte to form an ionic solution. The resistance of the solution remained too high for electrolysis.

2.1.4. Choice of Electrodes and Switching Electrodes

In early work, we used a copper foil as the anode, and a platinum gauze as the cathode. The foil quickly broke apart, as the solution surface stopped the electrolysis. A solid copper rod (oxygen free, 1/4 in. diameter) had sufficient strength to use as the anode.

Ultimately, two copper rods were used as the anode and cathode. Throughout the work, the anode formed a dense, dark resistive coating, which eventually stopped the current flow. By switching the electrodes, the current would again flow. Apparently, reversing the current helped break off the coating, which then fell off the electrode. By having two copper electrodes, oxidation of the copper would always be occurring, while the other would be cleaning. Running at ~50 mA, the electrodes were switched every 2 to 3 h by a timer. This switching permitted the electrolysis to run nearly continuously, day and night, to collect sufficient product.

Having established one set of conditions under which a continuous electrolysis would be established, several syntheses were done. Running in pure isopropanol, at 50 mA, with about 10 mM TBA-BF₄ electrolyte, a gas bubble was evolved about every coulomb, which was consistent with the approximate volume of the bubble. Thus H₂ was evolving quantitatively, within approximations. The solution first became faint straw

yellow, then darkened as an insoluble flocculent dark green material formed in the solution and on the anode. In a few cases, the coatings bridged the 3 to 5 mm gap between the electrodes. This bridge was knocked off by pushing the electrodes apart.

Electrolysis run of 1 to 3 days produced a large volume of dark green material in the bottom of the flask. The material was very flocculent, and easily stirred into solution. The filtered material was very dark green, almost black, with a muddy texture. Pumping on the material for 12 to 48 h reduced its volume greatly to only 10% to 20% of the filtered volume. The solid was dark, but some turquoise spots were visible.

2.1.5. Characterization of Green-Black Product

The dark green solid was virtually insoluble in isopropanol, but dissolved readily in ammoniated isopropanol to form a deep green-black solution. Dilution gave a light yellow-green. This light yellow-green is not the blue formed by ammoniating cupric methoxide, nor the blue of copper tetraamine. Addition of water caused no change in color over 24 h. (Heating the solution with water gave a precipitate within 30 min.) Addition of HCl resulted in an immediate color change to faint blue.

The slow hydrolysis behavior of the ammoniated solution, compared to the rapid acid hydrolysis had been seen earlier for copper methoxide. However, the light yellow-green solution is not comparable to the copper methoxide solution.

Elemental analysis for copper and carbon were done on the "muddy" solid and on samples of the vacuum dried solid (see Table 2-1). The dramatic increase in copper content upon vacuum drying of this sample was surprising. The closest explanation to this data is that a dialcoholate of CuF_2 or CuO was present in the "muddy solid," and the solvating alcohol was removed under vacuum to form CuF_2 or CuO . CuF_2

TABLE 2-1
CHEMICAL ANALYSIS OF COPPER ISOPROYOXIDE

Compound	Cu	C	C/Cu
$\text{Cu}(\text{OC}_3\text{H}_7)_2$	35.00	39.66	6.0
Muddy	28.6	28.0	5.18
Vacuum dried I	51.3	13.8	1.42
Vacuum dried II	69.5	7.4	0.56
$\text{Cu}(\text{OH})_2$	65.1		
CuO	79.7		
CuF_2	62.6		
$\text{Cu}(\text{C}_3\text{H}_7\text{OH})_4\text{F}_2$	18.6	42.4	
$\text{Cu}(\text{C}_3\text{H}_7\text{OH})_2\text{F}_2$	28.7	32.5	
$\text{Cu}(\text{C}_3\text{H}_7\text{OH})_2\text{O}$	31.8	36.1	
$\text{Cu}(\text{lactate})_2$	26.3	29.8	

does have a dihydrate, which is blue. Alternatively, copper lactate $[\text{Cu}(\text{C}_3\text{H}_4\text{O}_3)_2]$ may be the muddy species, although it is difficult to see how vacuum would remove the organic group. It is also difficult to see how oxidation of isopropanol would form lactic acid, in the absence of O_2 or H_2O .

This peculiar elemental analysis data, unexpected color of the ammoniated solution and the apparent low yield of solid product, after vacuum drying process, raises many unanswered questions. However, it is clear that the described electrochemical method to produce copper isopropoxide in high yield and purity in accordance with the described (Ref. 1) method was unsuccessful.

2.1.6. Electrolysis in Ethoxyethanol

Since other work is ongoing to make copper alkoxides from ethoxyethanol, electrolysis in this solvent was tried. TBA- PF_6 was used as the electrolyte. A blue material and a green material were formed in the cell, after an initial powder-puff blue material was formed. A blue solid was ultimately formed, which had a paste-like consistency upon filtration. Elemental analysis results are shown in Table 2-2. The blue powder may be an alcoholate of the alkoxide, although the content of copper and carbon seems low.

2.2. METAL ALKOXIDES PRECURSOR COMPOUNDS

2.2.1. Synthesis

During this reporting period, we have continued to study the synthesis reported by Payne (Ref. 2) and Mecartney (Ref. 3).

Homogeneous 123 precursor solutions are prepared in 2-ethoxyethanol using $\text{Y}(\text{OR})_3$, $\text{Ba}(\text{OR})_2$, and the soluble copper II mixed-ligand species $(\text{C}_5\text{H}_7\text{O}_2)_2\text{Cu}_2(\text{u-OR})_2$, where $\text{R} = \text{CH}_2\text{CH}_2\text{OCH}_2\text{CH}_3$ and $\text{C}_5\text{H}_7\text{O}_2 = 2,4$ pentanedione (acetylacetonone). The 2-ethoxyethoxo compounds were chosen instead

TABLE 2-2
 CHEMICAL ANALYSIS OF COPPER ALKOXIDE
 IN ETHOXYETHANOL

Compound	Cu	C	C/Cu
$\text{Cu}(\text{EtOEtO})_2$	26.31	39.74	8.0
I	8.7	37.4	22.7
II	7.5	36.5	25.7
$\text{Cu}(\text{EtOEtOH})_4(\text{EtOEtO})_2$	10.6	47.9	24.0

of the 2-methoxyethoxy compounds used by Payne in order to increase the solubility.

A difficulty with this synthetic procedure has been precipitation of a solid containing copper when the soluble Cu(II) species is added to the yttrium alkoxide. Payne suggests that this is due to an exchange of the acetylacetonate ligand on the Cu(II) species with the yttrium alkoxide. Rather than adjust the initial solution concentration by adding additional Cu(II) compound, we have been investigating the use of peroxides as stabilizing agents for the initial homogeneous solution.

2.2.2. Experimental

In order to study the effect that chemicals added during the hydrolysis and polycondensation of the starting alkoxides, have on the production of 123 powder we are using a fixed procedure. Typically, homogeneous solutions containing the 123 compounds are prepared by reacting 0.033 g (0.00024 mole) of barium granules (Alfa products) with 0.225 ml of a stock yttrium 2-ethoxyethoxide solution (0.00012 mole) and 0.275 ml dry 2-ethoxyethanol. The barium reacts completely in about 2 h at room temperature. To this solution is added 0.0914 g (0.00036 mole Cu) of the Cu(II) compound, which dissolves readily. After stirring at room temperature for 20 min, one to ten equivalents of water per mole of alkoxy ligand are added dropwise from a solution containing the water and additive in 2-ethoxyethanol. After an additional 1 to 4 h reaction time, the solvent is removed under vacuum at 55°C giving a black powder. The powder is dried in vacuum overnight at 130°C.

We are also conducting thermal gravimetric studies on the precursor powders in order to determine the effect of the additives on the decomposition behavior. These decomposition experiments are performed with a thermogravimetric apparatus (TGA) constructed at GA which can hold larger samples of powder than commercial TGA units. The powder sample is heated in a silver crucible suspended from the balance arm of a Cahn/

Ventron 1000 microbalance. The balance, contained in an enclosure, is connected to a quartz furnace liner. The liner is surrounded by a clam-shell furnace with MoSi_2 heating elements (applied test systems) and allows heating to 1200°C . The furnace temperature is controlled by a Micricon microprocessor connected to a single phase driver and silicon-controlled rectifier (SCR) (Eurotherm Corporation). Sample temperature is measured to $\pm 5^\circ\text{C}$ by a Type S thermocouple in an alumina sheath located about 0.25 in. from the sample. The weight of the sample and the temperature of the gas in close proximity to the sample is stored as a function of time on an IBM PC.

2.2.3. Results and Discussion

Table 2-3 describes the reaction conditions used during hydrolysis of the alkoxides. Since the minimum amount of water necessary for hydrolysis is 0.5 mole per mole of alkoxide moiety, water was used in excess. Hydrogen peroxide and t-butyl hydroperoxide were added to keep the copper in the Cu(II) oxidation state. Hydrazine was used in an attempt to reduce the copper acetylacetonate with the hope that decomposition to the 123 compound would occur at low temperature.

The stability of the solutions was estimated by observing the time from mixing necessary to observe a precipitate when a strong light beam was passed through the solution. Solutions without any additives generally showed a precipitate within 20 to 30 min from the addition of Cu(II) to the solution containing the Y and Ba alkoxide. When oxidizing agents are added to the solution, no precipitates are observed for 2 to 4 h after the addition (Table 2-4). Hydrazine, however, results in an immediate darkening of the solution and formation of a black precipitate. The use of hydrogen peroxide usually results in a product that, after calcining to 850, exhibits the diffraction pattern of only orthorhombic 123 (Table 2-4). When hydrozine is used, orthorhombic 123 is the major product, but the diffraction pattern of an impurity is also observed with a d-spacing of 2.7 to 3.2. It is difficult to identify

TABLE 2-3
MOLAR RATIO OF ADDITIVES USED DURING HYDROLYSIS
AND POLYCONDENSATION OF ALKOXIDES

Test	Expected Y:Ba:Cu	Additive Mole/Mole Alkoxide Moiety				
		H ₂ O	H ₂ O ₂	C ₄ H ₉ OOH	NH ₂ NH ₂	H ⁺
10094-4	1:2:3	1.7			1.1	
10094-11	1:2:3	4.5	0.17			
10094-15	1:2:3	3.0			1.7	
10094-31	1:2:3	6.5	0.11		2.1	
10094-51	1:2:3	3.6		0.43		
10094-89	1:2:3	4.5	0.16			
10094-70	1:2:0	4.2	0.15			
10094-82	0:0:1	4.5	0.17			
10096-9	1:2:3	3.9				0.07
10096-13	1:2:3	3.9				1.0
10096-16	1:2:3	3.9				0.07

TABLE 2-4
 STABILITY AND PRODUCTS OF HYDROLYZING SOLUTIONS
 OF 123 ALKOXIDES WITH ADDITIVES

Test	Solution Stability (h)	Measured ^(a) Y:Ba:Cu	Products ^(b)
10094-4	0		123 (211,011)
10094-11	4		123
10094-15	0	1:2.4:4.0	123 (211,011)
10094-31	4	1:2.0:3.8	123 (211,011)
10094-51	2	1:1.5:2.3	123 (211,011)
10094-89	2	1:2.1:3.8	123 (211,011)
10094-70	0		BaCO ₃ (Y ₂ O ₃)
10094-82	0	0:0:1	CuO
10096-9	3	1:2.1:3.7	123
10096-13	0		123 (211,011)
10096-16	3		

(a) Measured by EDAX.

(b) Measured by X-ray diffraction.

this impurity, but it may be a combination of the 211 and the 011 compounds.

In an attempt to understand the decomposition and conversion of the initial powder to the 123 compound, we have been measuring the weight loss of the samples as a function of the decomposition temperature (TGA). A comparison of the TGA for different hydrolysis additives is shown in Fig. 2-1. Typically, there are two areas of rapid weight loss. The high temperature region occurs between 750° and 850°C and does not depend on the additive used during hydrolysis. The low temperature region, however, occurs between 300° and 350°C for samples treated with hydrazine, and between 150° and 250°C for processes using oxidizing additives.

The weight loss is significantly smaller for processes in which hydrazine has been added. This suggests that the hydrazine reacts with Cu(II) compound liberating a high volatility material that is removed during the drying step, before the TGA run is conducted.

The TGA of a sample of hydrogen peroxide processed $YBa(OH)_x$ and $Cu(OH)_y$ is shown in Fig. 2-2. The powder produced when the Cu(II) compound is hydrolyzed in the presence of hydrogen peroxide decomposes below 200°C. The rapid weight loss was caused by an exothermic reaction which was observed using differential thermal analysis (DTA). The decomposition behavior of the powder produced when a mixture of the yttrium and barium alkoxides is hydrolyzed in the presence of hydrogen peroxide resembles the hydrazine attacks on the copper compound, releasing a volatile material which is removed during drying.

Since low temperature processing is desirable, one test (Fig. 2-3) was conducted in which a hydrogen peroxide processed sample was heated to 350°C and held isothermally for about 2000 min. The temperature was then increased to 850°C. The weight lost at 350°C reached a plateau which was similar to the weight lost during a continuous increasing temperature ramp. Furthermore, on increasing the temperature, additional

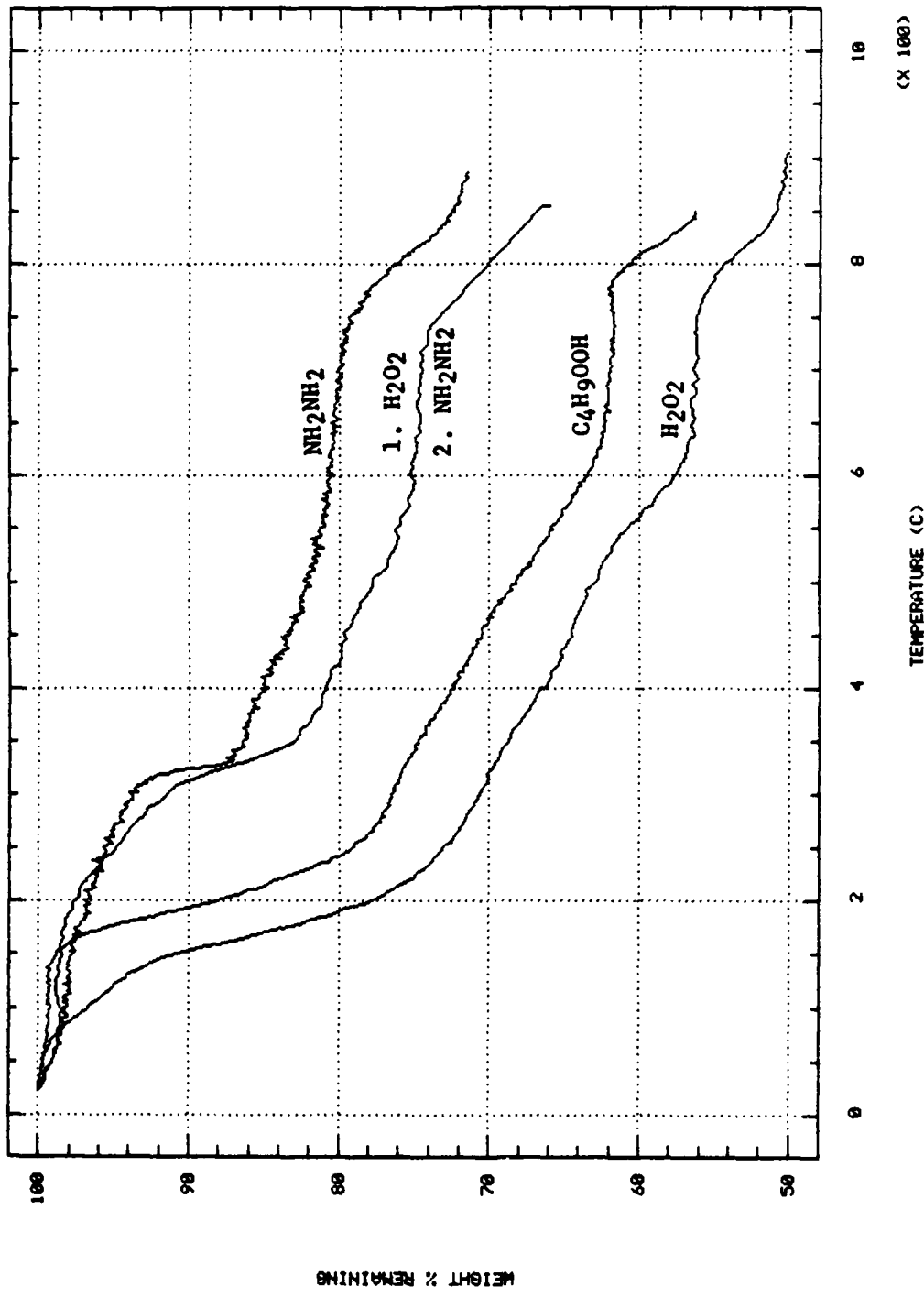


Fig. 2-1. Comparison of thermal decomposition of 123 precursor powders produced with additives during the hydrolysis step

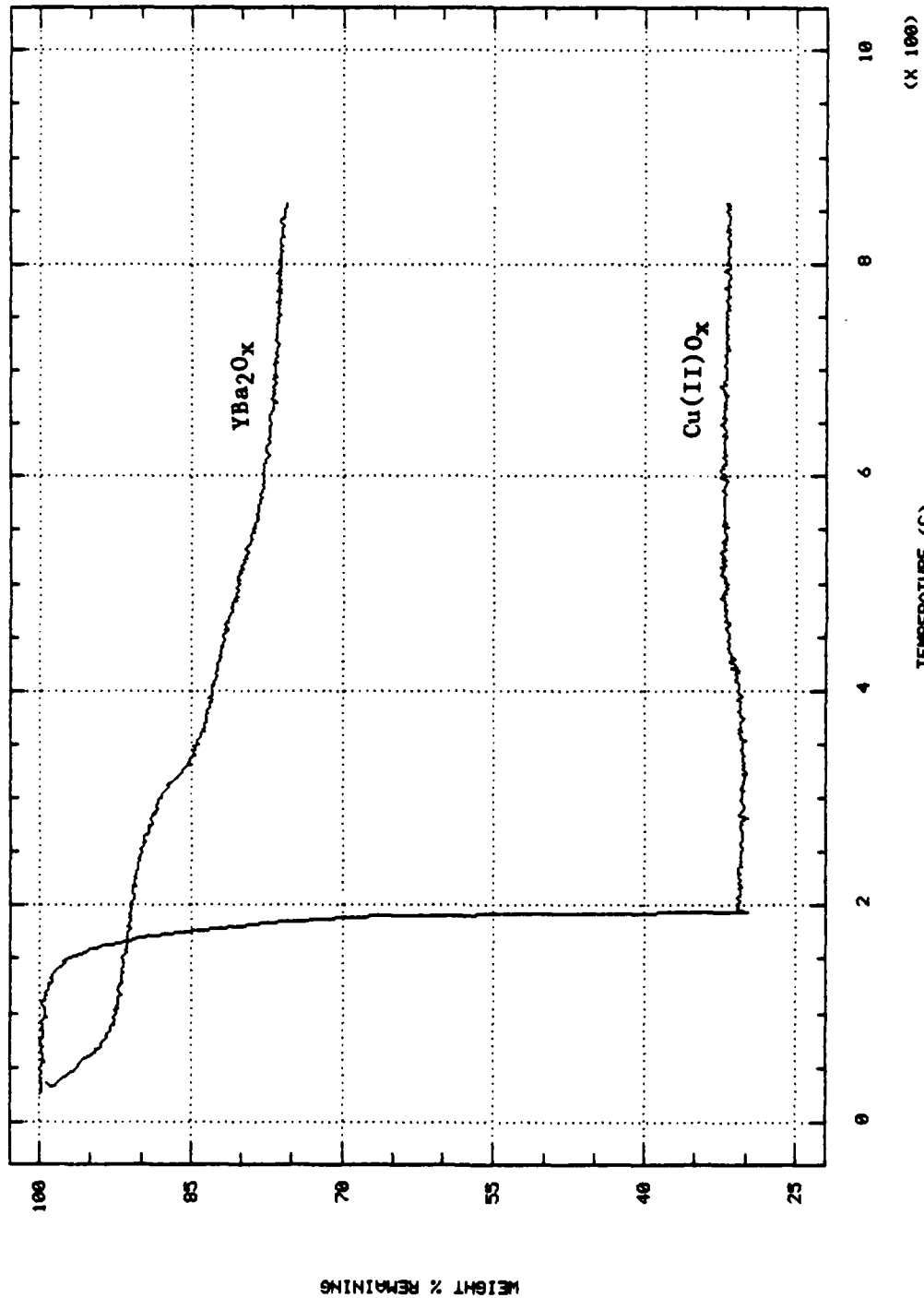


Fig. 2-2. Thermal decomposition of powders produced by hydrolyzing Y/Ba alkoxide and Cu(II) compound in presence of H₂O₂

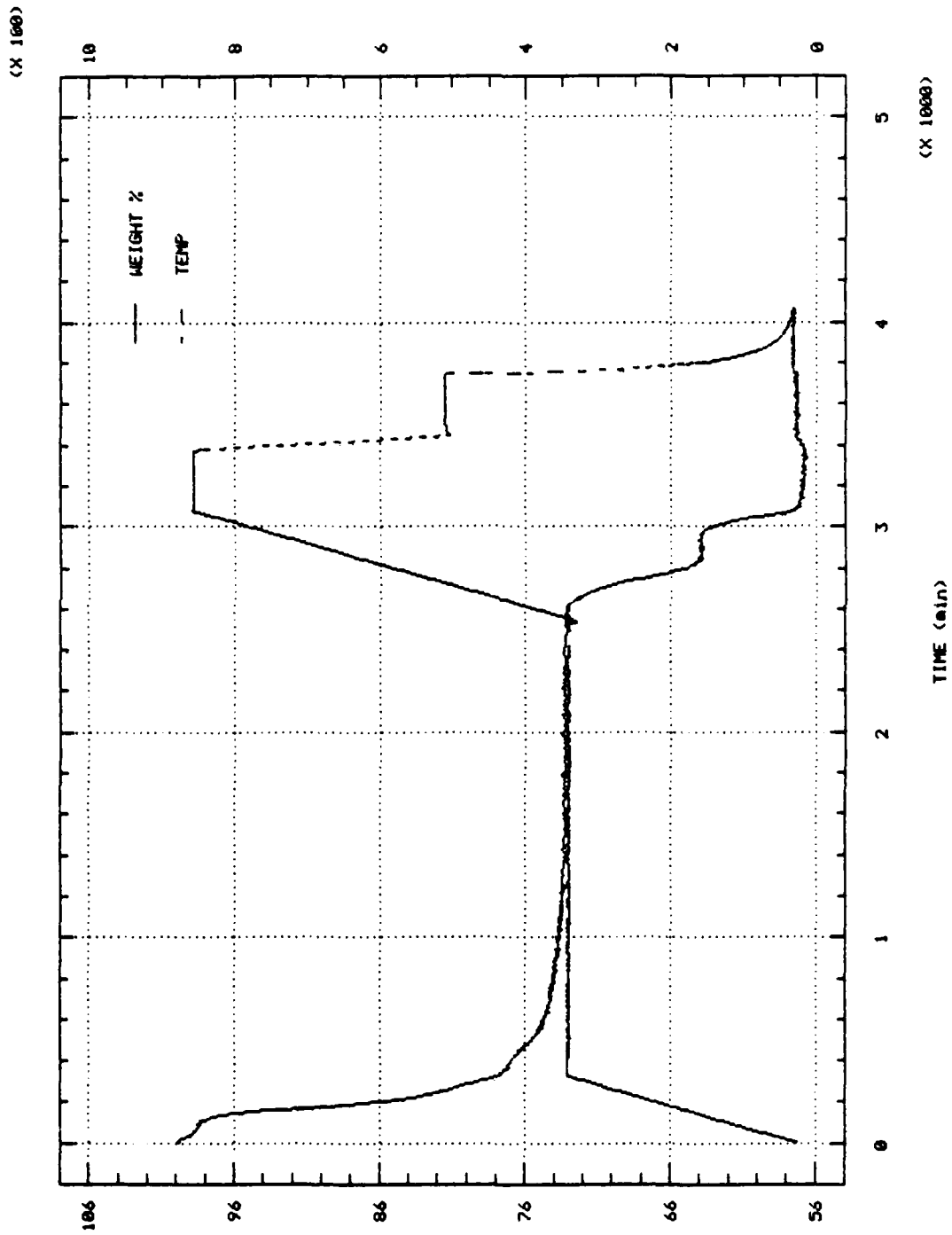


Fig. 2-3. Weight loss during ramp and hold test of 123 precursor powder prepared using H₂O₂ additive

weight loss occurred. Currently experiments are underway to determine the product composition in the different temperature regions.

An important goal of this work is to produce superconducting thin films. Accordingly, we have initiated experiments to develop thin films. A polished yttria stabilized zirconia (YSZ) disk has been coated with a discontinuous film of approximately the correct composition. This was accomplished by multiple dipping into a homogeneous solution of the starting materials that had been hydrolyzed in the presence of a catalytic amount of nitric acid (test 10096-16 in Tables 2-3 and 2-4). In between dips, the solution was allowed to air dry a few seconds, and then was heated to 130° and 170°C in the hot air from a heat gun. Because of the rapid drying, the film produced using this manual process shrunk three-dimensionally resulting in a "mud flat" appearance. Figure 2-4 is a scanning electron microscopy (SEM) photograph of the film. The flats were uniform in thickness and exhibited a smooth surface. An apparatus is being constructed which will allow automated dipping and control of the drying process.

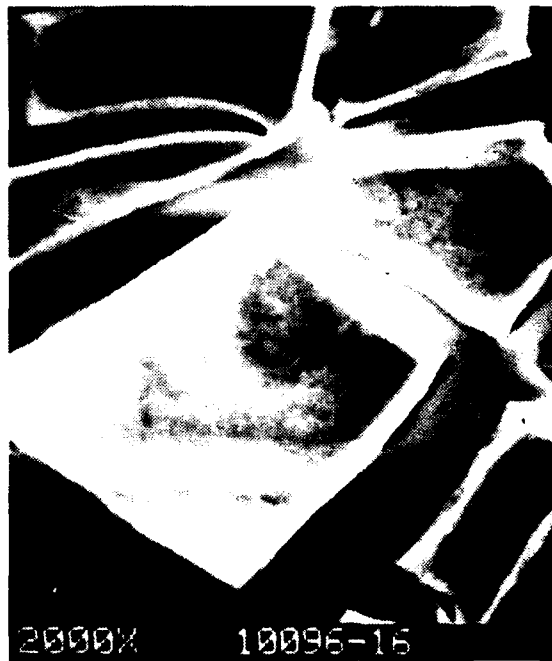


Fig. 2-4. SEM photographs of film produced by dip coating and rapid drying at 130° and 170°C

3. FIBER HEAT TREATMENT

3.1. OPTIMIZATION OF FIBER HEAT TREATMENT SCHEDULE

Optimization of heat treatment schedule for 123 fiber with adequate mechanical strengths as well as acceptable electrical properties is being continued. As stated in the previous report, the fiber integrity and fiber shape and morphology are strongly influenced by the organic removal rate between 200° and 500°C. The ideal conditions for organics removal of any preceramic fiber should be slow decomposition and diffusion rather than rapid removal of volatile species from the interior of the fiber. Since the organic pyrolysis is a kinetic process, both temperature and time need to be determined.

From TGA study, most of the organic pyrolysis occurs between 200° and 400°C (see previous report). Considerable weight loss occurred from 220° to 360°C at a 10°C/min heating rate in flowing oxygen. To determine the time needed to slowly remove the organics in the as-drawn fiber at this temperature range, isothermal TGA has been performed on 0.5 to 1 mm diameter fibers from 200° to 500°C at 50°C intervals for 2 h at each temperature in flowing oxygen. The objective of this experiment was to learn the time needed to reach a constant weight at each temperature. Figure 3-1 shows that the isothermal weight losses at 200° and 250°C did not reach constant values even after 2 h. It also shows that the weight losses at these two temperatures account for a substantial portion of the total weight loss. This indicates the heat treatment below 250°C is critical for the slow decomposition and diffusion of the organic species. A longer hold, 5 h at these two temperatures revealed that the weight losses at 200° and 250°C have not yet reached a constant weight (Fig. 3-2). Therefore, even longer time may be needed at these two temperatures. Additionally, it should be noted that the time needed

Sample: 9997.828
Size: 10.1680 mg
Method: 2 HRS/TEMP
Comment: O2 ATMOSPHERE 10°C/MIN

TGA

File: 1801.01
Operator: T. TAMORIA
Run Date: 22-Feb-89 16:31

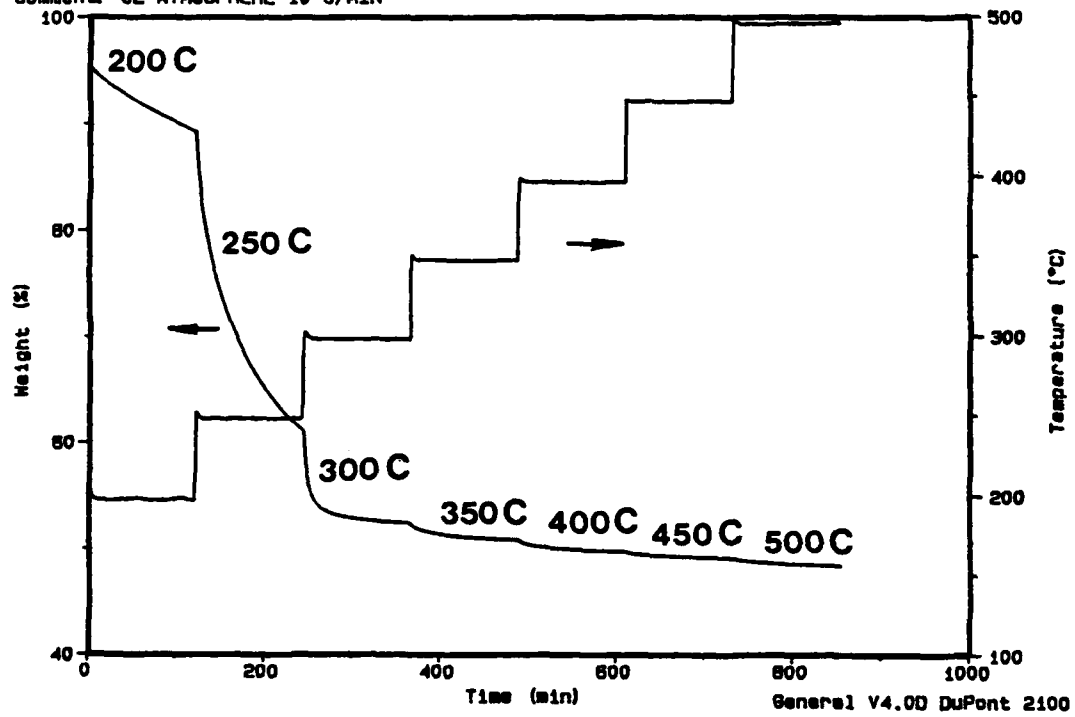


Fig. 3-1. Isothermal TGA on preceramic fiber (0.5 to 1 mm diameter) with 2 h at each temperature

Sample: 9997.928
Size: 11.1270 mg
Method: X HRS/TEMP
Comment: O2 ATMOSPHERE

TGA

File: 1813.51
Operator: T. TAMORIA
Run Date: 3-Mar-89 16:58

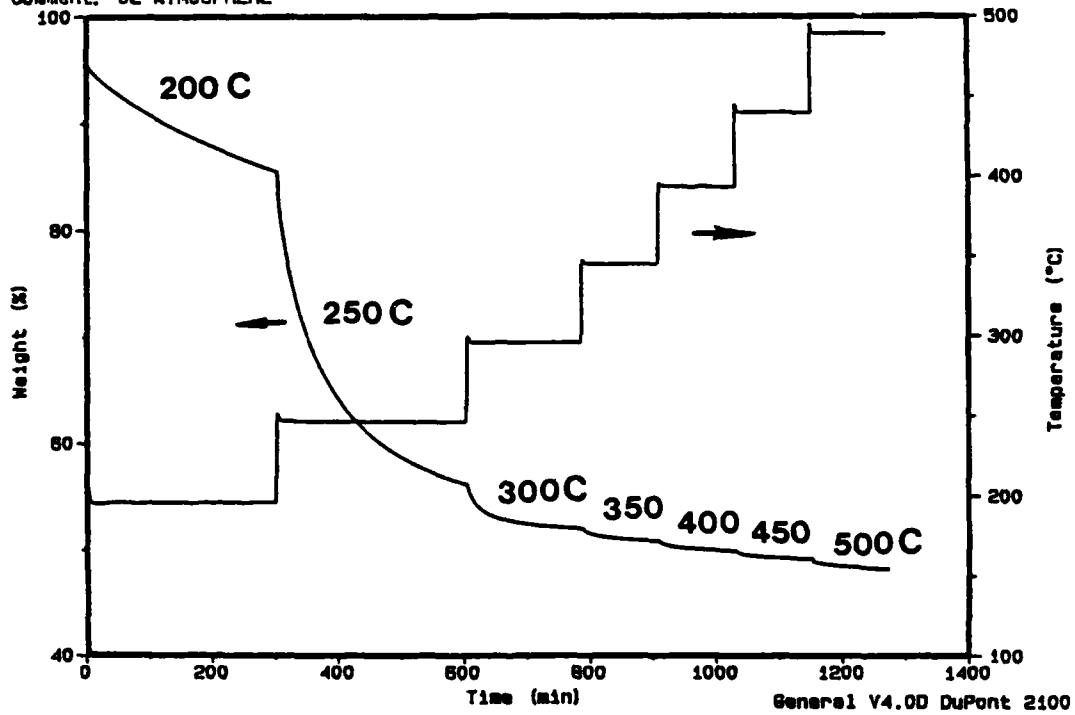


Fig. 3-2. Isothermal TGA curve of preceramic fiber for 5 h hold at 200° and 250°C and 2 h hold at 300°C and above

also depends on the fiber diameter. It is expected that the time required is shorter for thinner fibers. The prolonged time needed is thought to be due to the slow diffusion and decomposition of the organics from the interior of the fiber. The isothermal weight losses above 250°C reach constant weight within 1 to 2 h. Rapid heating rate in the range of 100° to 400°C generally produce a dense crust on the fiber surface with porous interior.

Heat treatment schedule between 600° and 900°C will depend on the time and temperature where a single phase $\text{YBa}_2\text{Cu}_3\text{O}_{7-x}$ with desirable microstructure can be obtained (either by direct crystallization from the amorphous phase or fine-scale solid state reactions). Systematic experiments were conducted to determine the crystalline phase at this temperature range. In order to distinguish the influence of the low temperature heat treatment (<400°C) from the higher temperature range, a fast heating rate is used (half an hour to reach the designated temperature) to study the phases existing between 700° and 950°C. Even though the experiment has not been completed at the present time, it can be seen that at 750°C, there are BaCO_3 and other phases, such as $\text{Y}_2\text{Cu}_2\text{O}_5$, present for 1 h heat treatment [Fig. 3-3(a)]. However, $\text{YBa}_2\text{Cu}_3\text{O}_{7-x}$ phase appeared for only 2 h of calcination [Fig. 3-3(b)]. After 4 h calcination, substantial amount of $\text{YBa}_2\text{Cu}_3\text{O}_{7-x}$ is present but the BaCO_3 is still present [Fig. 3-3(c)]. BaCO_3 persists as impurity at 800°C for 1 h but almost completely decomposes after 4 h [Figs. 3-4(a) and 3-4(b)]. At 850°C for 4 h, except for a small amount of Y_2BaCuO_5 , only $\text{YBa}_2\text{Cu}_3\text{O}_{7-x}$ phase is present [Fig. 3-5(a)]. Single phase of $\text{YBa}_2\text{Cu}_3\text{O}_{7-x}$ can be obtained, as described in the previous report, at 900°C for 4 h [Fig. 3-5(b)]. The tentative time-temperature-phase diagram for the appearance of $\text{YBa}_2\text{Cu}_3\text{O}_{7-x}$ phase is shown in Fig. 3-6. The present research goal is to determine the shortest temperature and/or time boundary for the 100% $\text{YBa}_2\text{Cu}_3\text{O}_{7-x}$ phase. Though, the time required for obtaining single phase $\text{YBa}_2\text{Cu}_3\text{O}_{7-x}$ may be greater than 4 h, it is presently believed that the time required for the full-densification, which is being studied separately, is the determining factor for eventually choosing the time and temperature profile for the fiber processing.

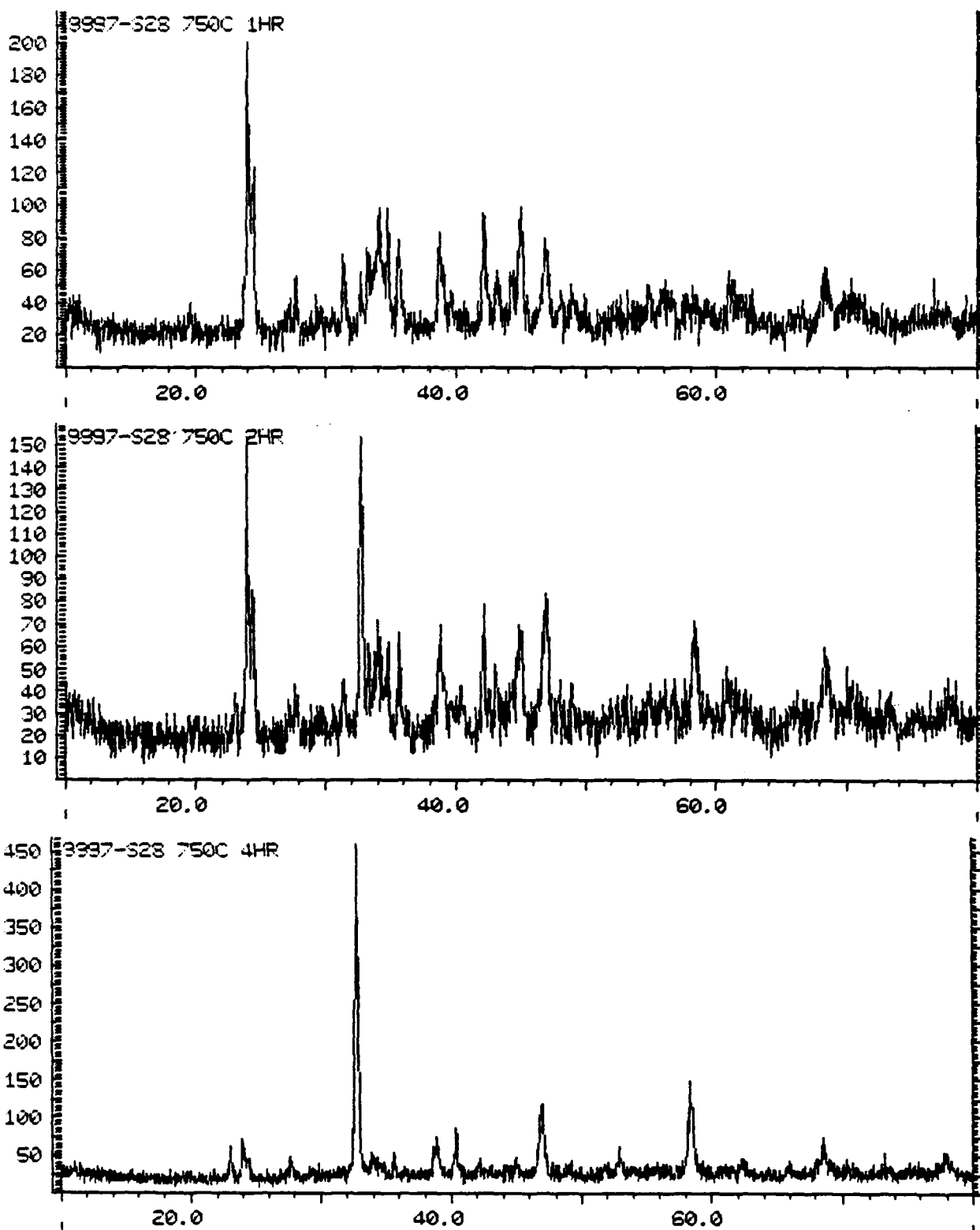


Fig. 3-3. X-ray diffraction of fiber calcined at 750°C for (a) 1 h; (b) 2 h; and (c) 4 h

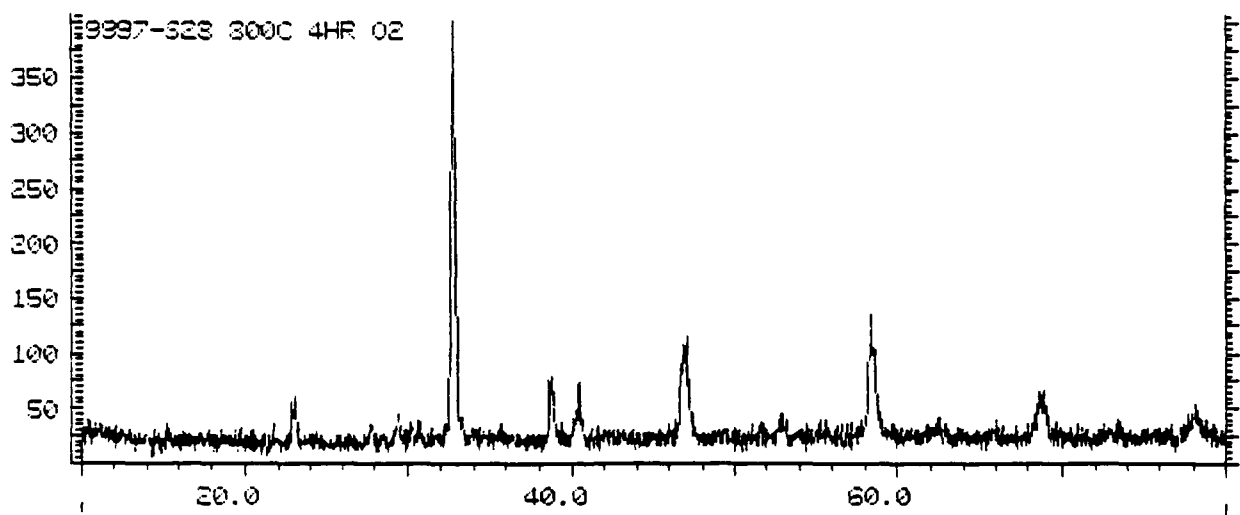
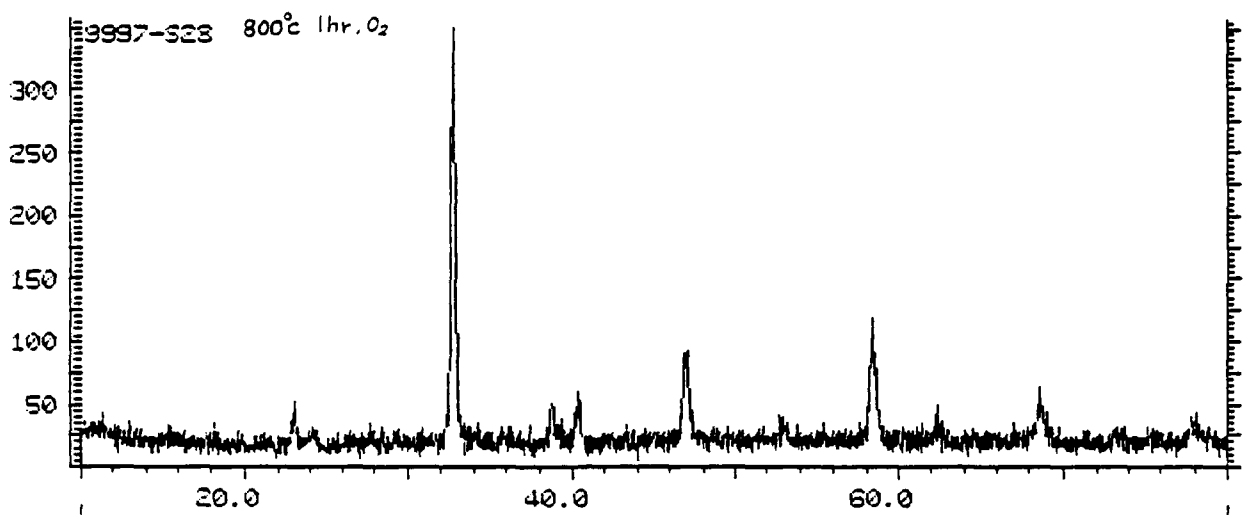


Fig. 3-4. X-ray diffraction of fiber calcined at 800°C for (a) 1 h;
(b) 4 h

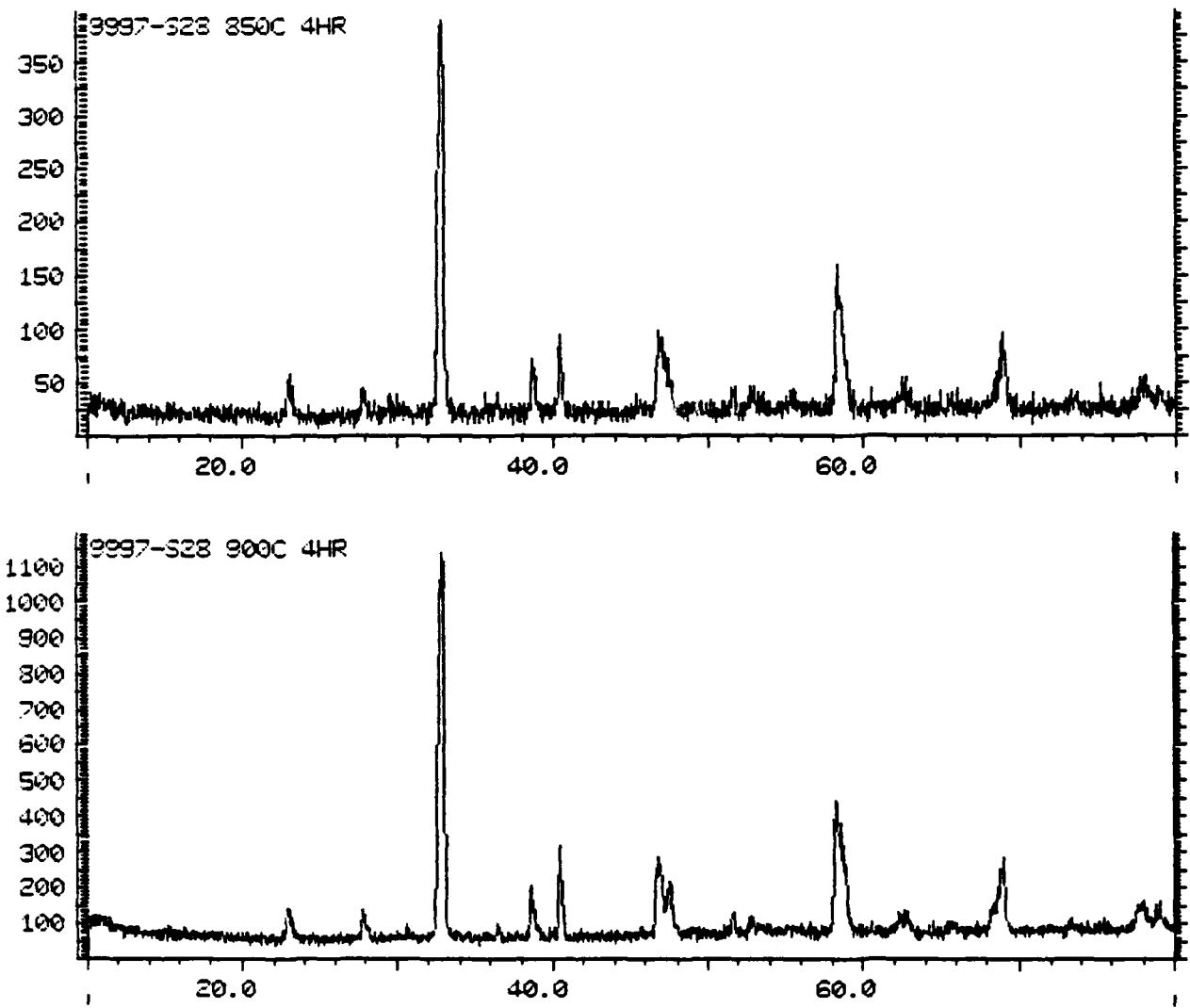


Fig. 3-5. X-ray diffraction of fiber heat-treated at (a) 850°C for 4 h and (b) 900°C for 4 h

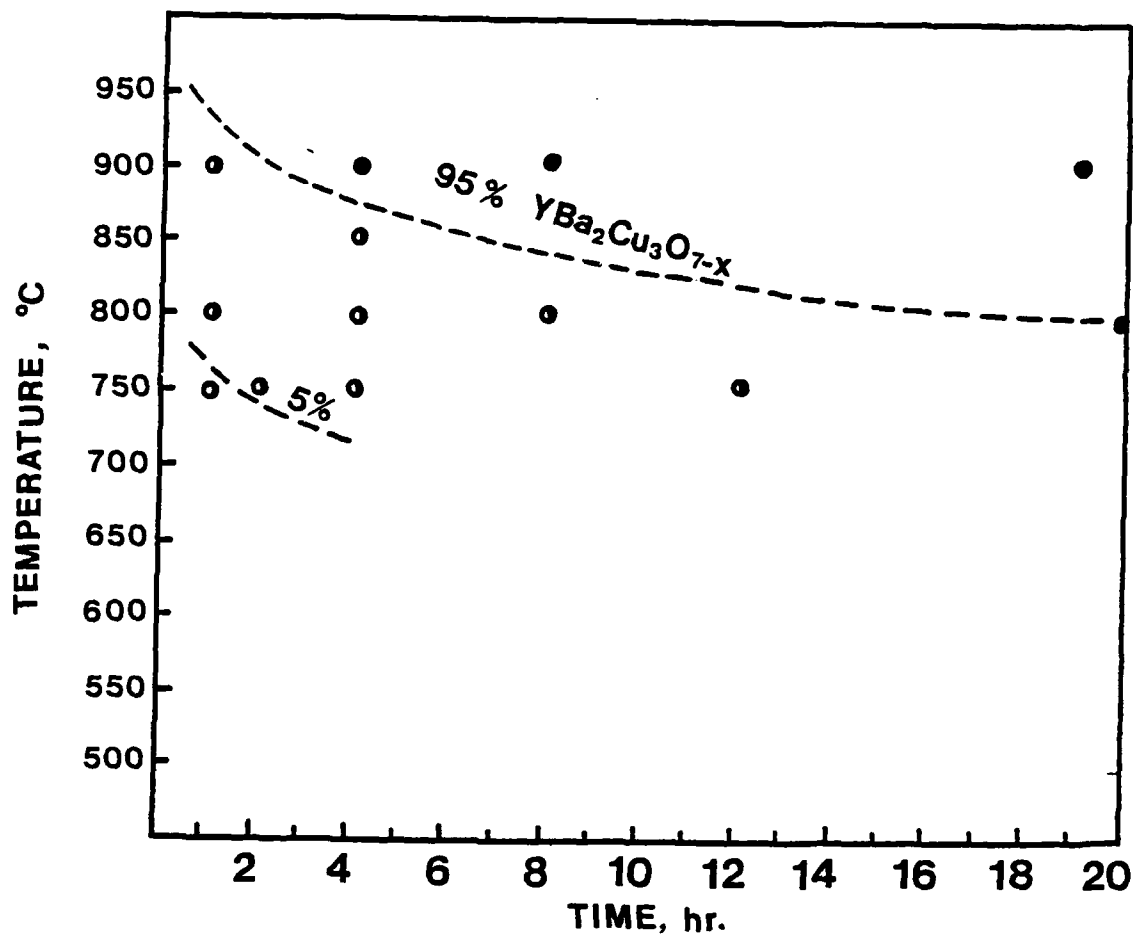


Fig. 3-6. Time-temperature-phase diagram for the formation of YBa₂Cu₃O_{7-x} phase

By stepwise heat treatment below 500°C and slow heating from 500° to 900°C, dense crust and hollow core morphology of the sol-gel derived fibers have been suppressed and more or less uniform porous fibers have been obtained (Fig. 3-7). It is clear that the same density throughout the fiber cross section is required before final densification heat treatment, in order to prevent differential sintering.

The heat treatment schedule will be extended beyond 900°C, from 870° to 1000°C in order to determine the optimum temperature and time needed where full-densification can be achieved with no exaggerated grain growth. It has been found, by others, that abnormal grain growth occurs when the fiber is heated above 920°C. Fibers made under this program which have been heat treated to 970°C, 2 h, exhibit faceted crystals and are mechanically weak (Fig. 3-8).

3.2. CONTINUOUS FIBER DRAWING DEVELOPMENT

Fiber drawing equipment has been completed to study the conditions, including the solution concentration, viscosity, evaporation of solvent, drawing speed, etc., required for the continuous drawing process. The conditions for hand-drawing and mechanical-drawing require different solvent evaporation rate. Continuous fibers have been successfully drawn from the solution by either up-drawing [Figs. 3-9(a) and 3-9(b)] or down-drawing techniques (Fig. 3-10). The fiber diameter can be varied depending on the up- or down-drawing speeds and/or diameter of the spinneret.

3.3. FIBER PREFERRED CRYSTALLOGRAPHIC-ORIENTATION DEVELOPMENT (TEXTURING)

Due to the anisotropy of orthorhombic $\text{YBa}_2\text{Cu}_3\text{O}_{7-x}$ crystal, the electrical conducting properties are strongly orientation dependent. It has been shown that it is necessary to align the crystals with their a-b plane parallel to and their c-axis perpendicular to the fiber axis in order to maximize the critical current density. Preferred orientation

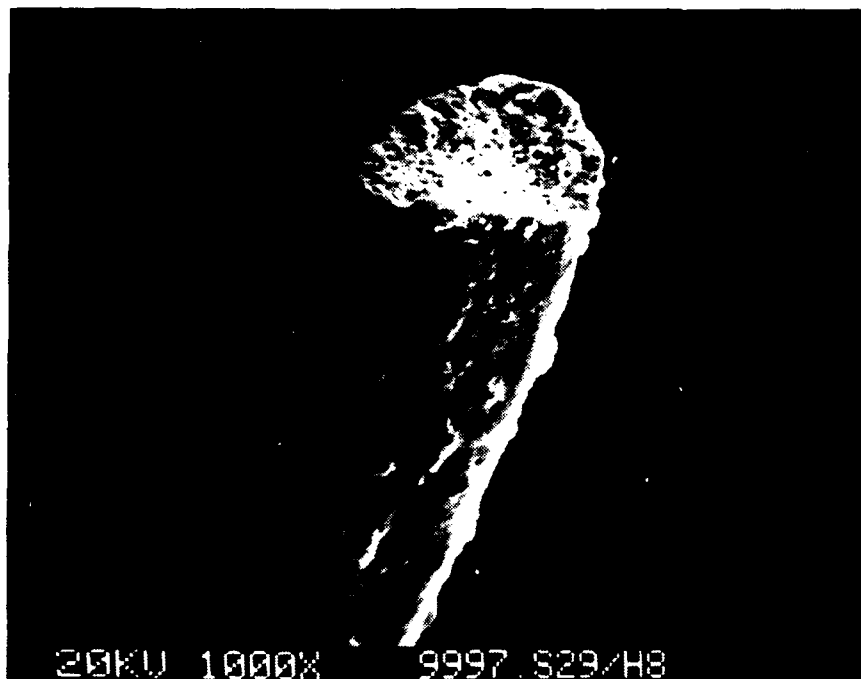


Fig. 3-7. SEM micrograph of $\text{YBa}_2\text{Cu}_3\text{O}_{7-x}$ fiber with stepwise annealing below 450°C and maximum calcining temperature of 900°C , 3 h showing more uniform density distribution in the cross section



Fig. 3-8. SEM micrograph of YBa₂Cu₃O_{7-x} fiber calcined stepwise below 450°C and with maximum annealing temperature of 970°C, 2 h showing excess grain growth

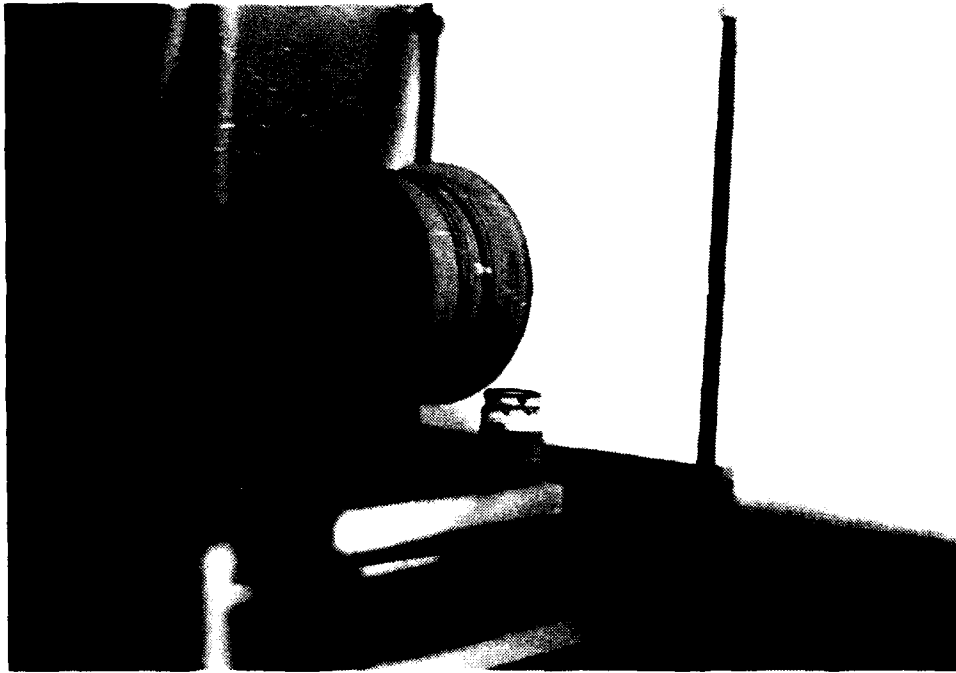


Fig. 3-9(a). Continuous preceramic fibers mechanically drawn (up-drawing method) from the polymeric solution

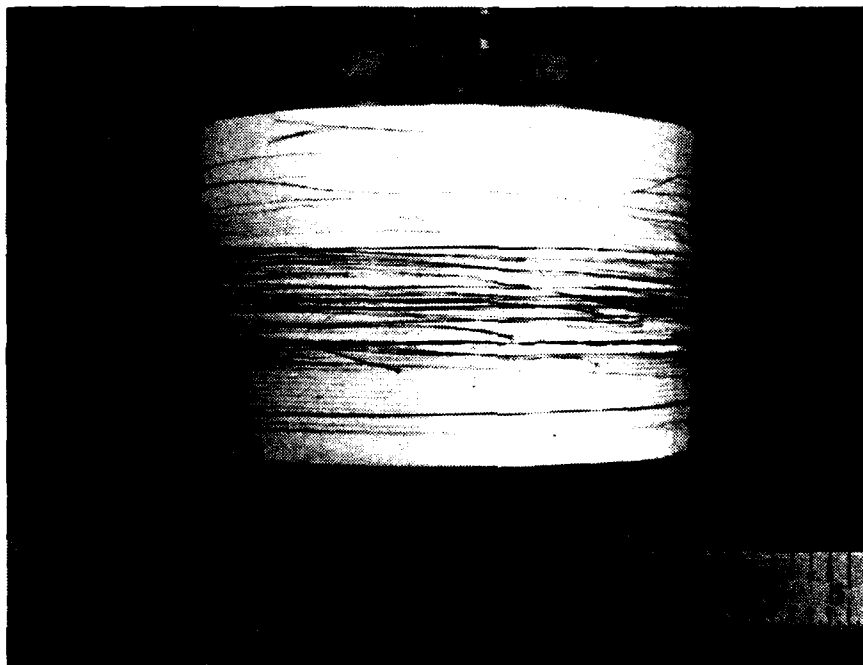


Fig. 3-9(b). Continuous preceramic fiber spool prepared by the up-drawing method



Fig. 3-10. Continuous preceramic fiber prepared by the down-drawing and extrusion method

can be achieved in metallo-organic derived $\text{YBa}_2\text{Cu}_3\text{O}_{7-x}$ fibers either by melt-texturing, heterogeneous nucleation through seeding with the help of magnetic field or surface crystallization.

The heterogeneous nucleation through seeding the fine crystallites with the assistance of magnetic field alignment will first be tried. In order to seed the viscous solution, fine crystallites size 123 should first be produced. For a fiber of 20 to 50 microns of final diameter, the seeds should be well below the micron-size, nonagglomerated, and well-crystalline. Large seeds will generate rough surface as well as enhance the secondary grain growth in the fiber. These will surely deteriorate fiber mechanical strength.

Fine crystals of $\text{DyBa}_2\text{Cu}_3\text{O}_{7-x}$ have been successfully produced by pyrolysis of paper filament coated with metallo-organic solution (prepared by the same method as described in previous reports). The goal is to produce highly crystalline submicron 123 particulates by gentle crushing of the fiber formed. The experimental results indicate that the nucleation and growth of the powder is suppressed even after prolonged firing at 850° to 950°C . While the crystallinity is improved, and well-developed crystal facets are achieved by prolonged firing.

Several $\text{DyBa}_2\text{Cu}_3\text{O}_{7-x}$ powders after firing at different temperature and time are shown in Figs. 3-11(a) and 3-11(b). In some areas where solution is trapped by the capillary force the grain growth is more prominent [Figs. 3-12(a) and 3-12(b)]. This implies a very dilute solution coated paper filaments may be used as a potential source for 123 fine crystal as seed material. Detailed study is being performed to determine the best procedure for production of single-phase submicron $\text{DyBa}_2\text{Cu}_3\text{O}_{7-x}$ powder. The preliminary results indicate the crystallization is similar to that of $\text{YBa}_2\text{Cu}_3\text{O}_{7-x}$ (Fig. 3-13).

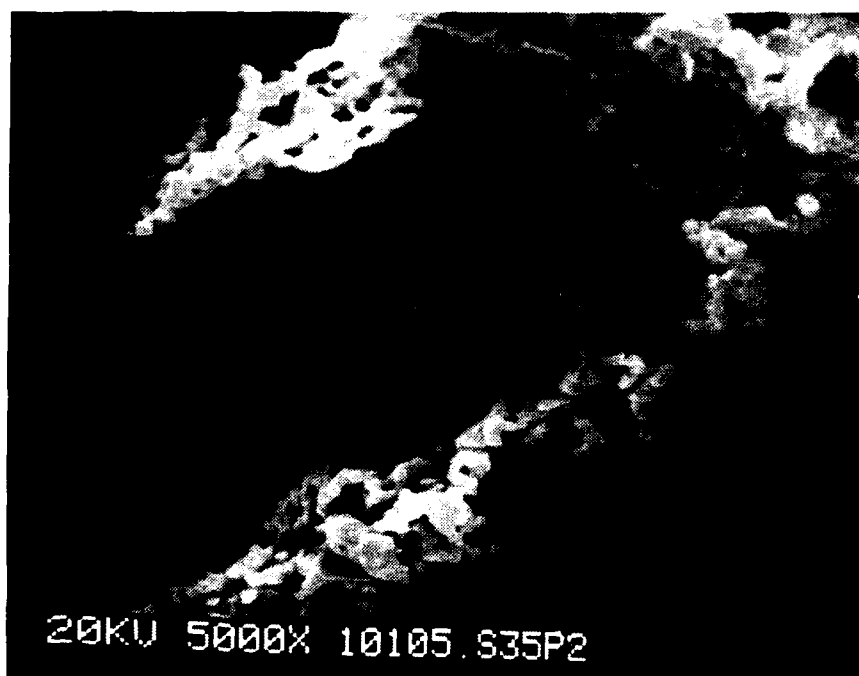
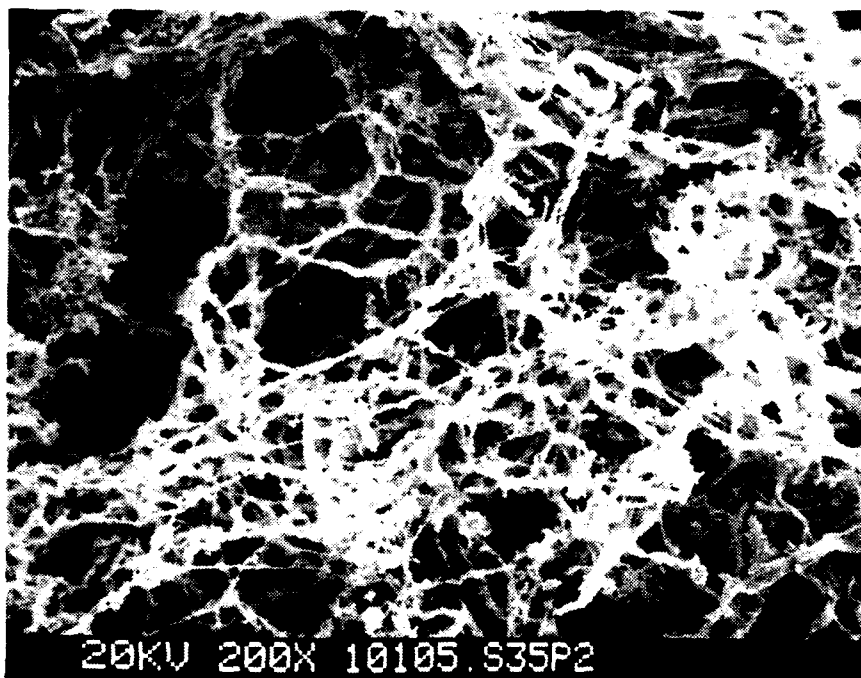


Fig. 3-11. (a) $\text{DyBa}_2\text{Cu}_3\text{O}_{7-x}$ powder prepared by the pyrolysis of solution coated on paper filaments and (b) a higher magnification shows the crystals are loosely agglomerated even after 900°C 4 h heat treatment

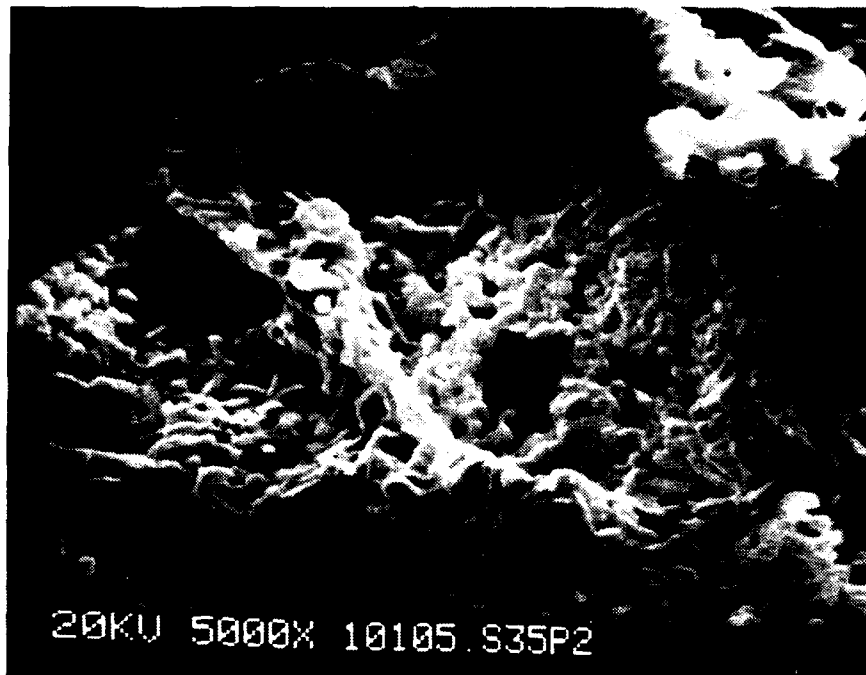


Fig. 3-12. DyBa₂Cu₃O_{7-x} powder calcined at (a) 900°C, 4 h and (b) 900°C, 8 h

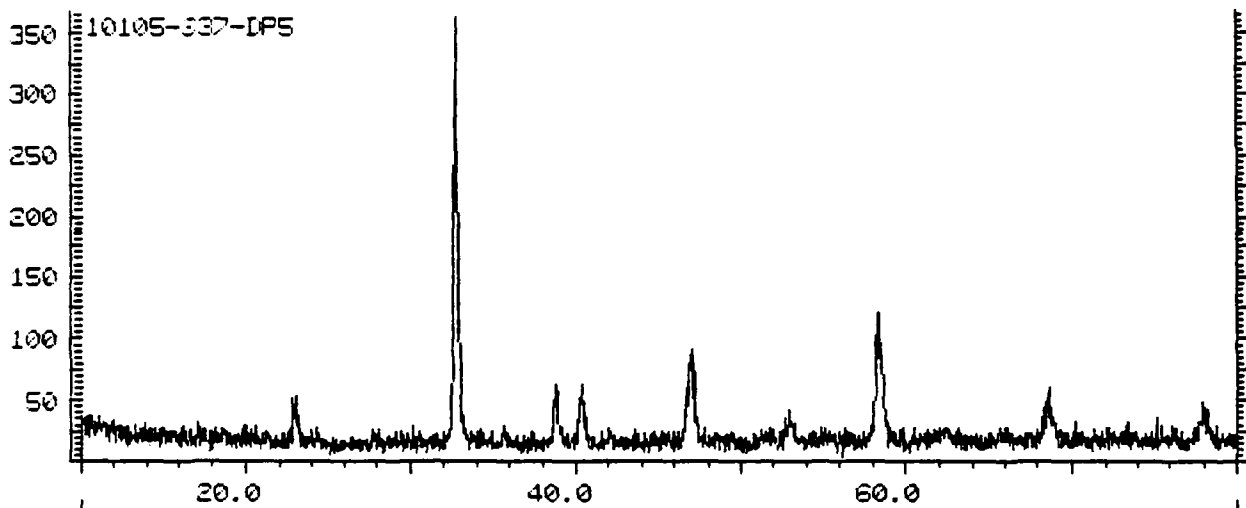


Fig. 3-13. X-ray diffraction of $\text{DyBa}_2\text{Cu}_3\text{O}_{7-x}$ powder calcined at 800°C , 16 h

3.4. THIN FILM PREPARATION

Thin films of 123 have been prepared by dipping thin disks of YSZ in the $\text{YBa}_2\text{Cu}_3\text{O}_{7-x}$ precursor solution. The disks have been coated 20 times then subsequently calcined at 900°C . This process cycle was repeated six times. The film is fairly uniform. X-ray diffraction indicates the crystalline phase is $\text{YBa}_2\text{Cu}_3\text{O}_{7-x}$ (Fig. 3-14). The microstructure and electrical properties are currently under investigation.

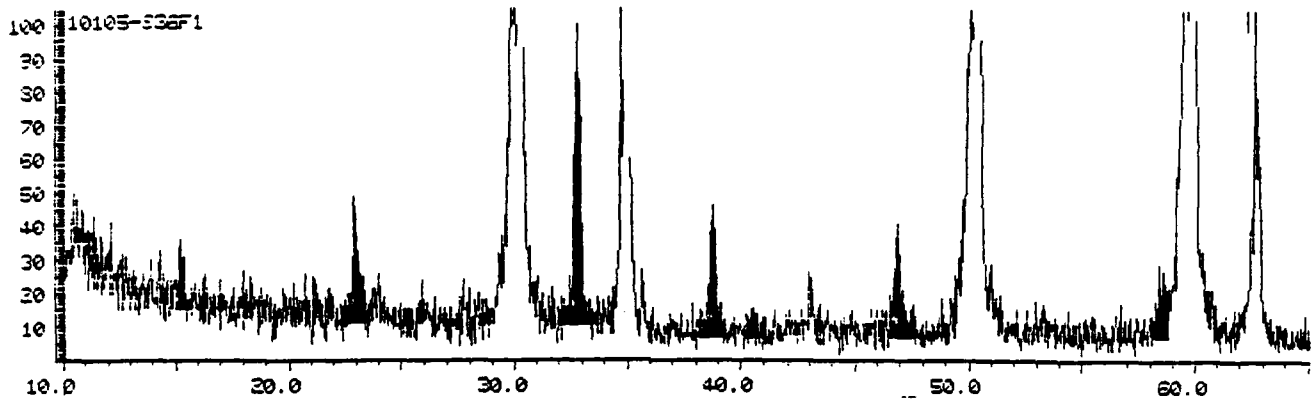


Fig. 3-14. X-ray diffraction of $\text{YBa}_2\text{Cu}_3\text{O}_{7-x}$ film on YSZ substrates (total soaking time at 900°C is 30 min after six processing cycles)

4. TECHNIQUE FOR MEASURING 123 RESISTIVITY AS A FUNCTION OF TEMPERATURE AT MICROWAVE FREQUENCIES

The measurement of 123 resistivity at microwave frequencies as a function of temperature can be accomplished by constructing a microwave cavity in which the walls are coated with the material under test. If the cavity is driven by an external source at a frequency corresponding to one of its natural resonant modes, energy is transferred between the electric and magnetic fields of the resonance. A certain fraction of this stored energy is dissipated each cycle into the resistivity of the walls via the radio frequency (rf) currents associated with the electromagnetic wave structure. A useful figure of merit is the cavity's quality factor, or Q, for the mode under question which is given by:

$$Q = 2\pi \frac{\text{Stored Energy}}{\text{Energy Dissipated per Cycle}}$$
$$= \omega \frac{U_{\text{stored}}}{P_{\text{dissipated}}}, \quad (4-1)$$

where ω is the radian frequency of the resonant mode of interest. Numerous methods exist in the microwave art of the measurement of cavity Q, some of which will be discussed below, however, all require that the user is aware of all power dissipation mechanisms involved, and not just the dissipative wall losses, and that proper experimental technique is followed to separate out these other loss mechanisms.

One difficulty in the implementation of high Q cavities is the prevention of rf leakage at the mechanical joints where the cavity is assembled. This occurs because almost all modes, regardless of cavity shape, contain electromagnetic fields whose resultant wall currents perpendicularly cross these joints in at least some regions. One

notable exception to this is the circular cylindrical TE_{0n1} family of modes. These modes are relatively insensitive to the tight tolerance fitting, joining, and clamping at the joints of other modes, even for high Q, low loss designs. This constructional advantage is particularly attractive for cryogenic designs which must undergo large temperature excursion. For these reasons, we intend to begin construction on a TE_{011} circular cylindrical cavity during the next reporting period.

The electric and magnetic fields (E and H, respectively) in the radial, azimuthal, and axial (r, θ , and z) directions for this cavity mode are given by:

$$E_{\theta} = E_0 J_1(k_c r) \sin(kz) e^{i\omega t} \quad , \quad (4-2)$$

$$E_r = E_z = H_{\theta} = 0 \quad , \quad (4-3)$$

$$H_r = -i \frac{k}{k_c} \frac{E_0}{Z_0} J_1(k_c r) \cos(kz) e^{i\omega t} \quad , \quad (4-4)$$

$$H_z = -i \frac{k_0}{k_c} \frac{E_0}{Z_0} J_0(k_c r) \sin(kz) e^{i\omega t} \quad . \quad (4-5)$$

The cutoff, free-space, and guide wavenumbers are given by:

$$k_c = \frac{3.8317}{a} \quad , \quad (4-6)$$

$$k_0 = \frac{\omega}{c} \quad , \quad (4-7)$$

$$k = k_0^2 - k_c^2 = \frac{\pi}{L} \quad , \quad (4-8)$$

for a cavity of radius a and length L. The free space impedance, $Z_0 = 377$ ohms and the Js are the familiar Bessel functions of the first kind of order 0 and 1.

From these fields, we can calculate the cavity's stored energy, U, the wall loss, P, and the resulting Q:

$$U = \frac{\epsilon_0 \pi a^2 L}{8} E_0^2 J_0^2(k_c a) \quad , \quad (4-9)$$

$$P = \frac{\pi a L}{4 k_0^2} \frac{E_0^2}{Z_0^2} R_s \left(k_c^2 + \frac{2a}{L} k^2 \right) J_0^2(k_c a) \quad , \quad (4-10)$$

$$Q = a \sigma R_s \frac{k_0^2}{k_c^2 + \frac{2a}{L} k^2} = \frac{a}{\delta_{skin}} \frac{k_0^2}{k_c^2 + \frac{2a}{L} k^2} \quad , \quad (4-11)$$

where R_s is the surface resistivity in ohms "per square," and the skin depth, δ_{skin} , is the e-folding distance for the rf wall currents into the imperfect conductor of conductivity σ .

We desire a test cavity with a TE_{011} resonance of 10 GHz. although not critical, we choose the aspect ratio, $a/L = 0.766$ to minimize the cavity's internal surface area for coating. This then implies an internal diameter of 4.32 cm and an internal length of 2.82 cm. A high purity copper cavity at room temperature ($R_s = 26 \text{ m}\Omega$) of these dimensions would have an expected Q of 28,000. work by Newman, et al. at NRL (APL 54, 389) showed an improvement of three in R_s for their high T_c material at 18 GHz. Since, as a first approximation, R_s varies as f^2 for a superconductor and as $f^{0.5}$ for conventional conductors, an improvement of 7.2, or $R_s = 3.6 \text{ m}\Omega$, might be expected for a similar experiment at 10 GHz. Since we intend to coat all internal conducting surfaces of our cavity, an overall Q of 200,000 is expected.

A troubling source of loss in many cavity Q measurements is the effect of the coupling probes or irises on the cavity resonance. This problem can be overcome by successively lessening the strength of the coupling. For example, using the two probe transmission method, the most familiar of the Q measurement techniques, if we desire a received signal strength of 1 mV from an HP 423B microwave detector diode, and

furthermore assume a weak coupling factor of 0.01 (probe losses 1% of wall losses) into our $Q = 200,000$ cavity, a maximum H field of 11 A/m is developed on the superconductor and a source strength of 30 mW would be required, a level certainly feasible and requiring little amplification from commercial X-band synthesized signal generators.

Alternately, we could use a modification of the single port impedance technique of Q measurement (which reduces the complexity of the cryostat design) and measure the full width at half maximum of the reflected signal as the coupling is increased. At the critical point at which no reflection is detected, the measured Q is half of that due to wall losses alone and much smaller signal strengths are involved.

Barring any theoretical constructs that may limit our Q to 200,000, even higher Qs may be obtainable with improvements in coating purity and surface preparation. (Superconducting niobium cavities for use in particle accelerator research have demonstrated Qs of 10^9 at these frequencies.) For such narrow bandwidths, the cavity Q is more easily measured in the time domain using the decrement method in which the ring-down time is measured following a pulsed stimulus.

5. THE EFFECT OF FLUX CREEP ON THE SURFACE RESISTANCE OF HIGH T_c SUPERCONDUCTORS

5.1. INTRODUCTION

Ceramic oxide superconductors have both low pinning strength, because of their short coherence length and low carrier density, and a high operating temperature compared to conventional superconductors. As a consequence, magnetic flux can creep by thermal activation over relatively low barriers. This phenomenon, which is relatively hard to detect in conventional superconductors (Ref. 4), can dominate the transport properties in the ceramic oxides (Ref. 5), as a result, one never achieves a true zero resistance state in these superconductors (Ref. 4), and the usefulness of these superconductors depends on the tolerance of flux motion in each specific application.

In the sections which follow, expressions are developed, roughly following the lead of the Anderson-Kim model (Refs. 6 and 7), which describe the effect of flux motion in the superconductors. As a result of two years of frantic work since the original discovery of these superconductors, most of the parameters in these equations are reasonably well known. One, the flux attempt frequency is not known, and will be used to fit the equations to reliable transport measurements. Finally, using the fitted equations, we make predictions about the surface resistance at high frequencies.

5.2. FLUX CREEP EQUATIONS

Here a line of analysis advanced by Anderson (Ref. 6) and Kim (Ref. 7) is used. Additionally, the discussions of Campbell and Evetts (Ref. 8) as applied to the ceramic oxide superconductors by Yeshurun and Malozemoff (Ref. 9) are heavily emphasized. However, for the purpose of

this discussion, the main theme of their argument is applied in a somewhat different direction by focussing on the relatively low field requirements for a cavity application, and by considering the effect of the flexibility of flux lines as defined by Campbell and Evetts (Ref. 8) and Kramer (Ref. 10).

The energy cost, U_{pin} , of moving a magnetic flux bundle from some pinning site, which is not superconducting, into a completely superconducting volume ought to scale with the energy required to force (from the presence of the flux bundle) some of the superconductor into the normal state (Refs. 4 and 9). The change in the superconducting volume is proportional to the volume of the pinning centers which the flux left behind. Their minimum size is set by the superconducting coherence length ξ , and the Helmholtz free energy density of an extreme Type II superconductor (the Ginzberg-Landau parameter $\kappa \gg 1$) has the form (Ref. 9)

$$-(f_s - f_n^h) = \frac{1}{2} \frac{\mu_0 (H_{c2} - B/\mu_0)^2}{[1 + (2\kappa^2 - 1) \beta_A]} \cong \frac{1}{2} \mu_0 H_c^2 (1 - h)^2, \quad (5-1)$$

where $H_{c2} = \sqrt{2\kappa} H_c$ is the upper critical field and H_c is the thermodynamic critical field, $h = H/H_{c2}$. The pinning energy is thus

$$U_{pin}^{point} = \frac{1}{2} \mu_0 H_c^2 \xi^3 (1 - h)^2. \quad (5-2a)$$

We assume that the pinning sites are present at a density of $1/d_{pin}^3$. If the minimum flexible length of a flux bundle, $s < d_{pin}$ (see Appendix A.1), then the flux bundle can hop from one pinning site at a time, and the activation energy for hopping is given by Eq. 2a. If $s > d_{pin}$, then the rigidity of the flux bundle forces it to hop from all the

pinning sites within that length, n_p , simultaneously, so Eq. 5-2a changes to:

$$U_{pin}^{point} = \frac{1}{2} \mu_0 n_p H_c^2 \xi^3 (1 - h)^2 \quad . \quad (5-2b)$$

That same rigidity prevents the bundle from being pinned except by sites within ξ of its flexing distance, d_{disp} . As a result, $n_p \approx 1$ up to $s_0 \approx d_{pin} (d_{pin}/\xi)^2$, and only then increases n_p as s/s_0 (see Appendix A.2). Hereafter, the flux lattice will be considered floppy if $s < d_{pin}$, and rigid if $s > d_{pin}$. In the latter case, the distance between effective pinning sites is increased to $d_{pin}^* \approx s$ up to $s = s_0$.

Now, suppose the superconductor carries a current J and the bundle contains a field B . then the flux bundle experiences a Lorentz force which tries to displace it from the pinning center. The pinning center experiences a force:

$$F_{magn} = BJA_s = J\Phi_0 d_{pin}^* \quad , \quad (5-3)$$

where $A = a_0^2$ is approximately the cross section of the flux lattice surrounding each bundle, and we assume that each bundle carries only one quantum of flux. The flux is shifted inside the pinning site until the restoring force caused by the gradient of the potential well restores equilibrium. It unpins only when the Lorentz force equals the maximum force exerted by the potential well, $F_{pin} \approx U_{pin}/\xi$. From that one gets

$$F_{pin} = J_c^0 \Phi_0 d_{pin}^* = U_{pin}/\xi \quad , \quad (5-4)$$

where $J_c^0 = U_{pin}/(\xi\Phi_0 d_{pin}^*)$ is the critical current in the absence of flux creep.

The current tilts the potential well of the pinning sites as shown in Fig. 5-1 so that

$$\begin{aligned} U^+(J) &= (U_{pin} + J\Phi_0 d_{pin}^*) \\ &= U_{pin} [1 + (d_{pin}/\xi) (J/J_c^0)] \quad , \end{aligned} \quad (5-5a)$$

$$U^-(J) = (U_{pin} - J\Phi_0 \xi d_{pin}^*) = U_{pin} (1 - J/J_c^0) \quad . \quad (5-5b)$$

When $J = J_c^0$, flux flows without a barrier - it need not be thermally activated, and the flux motion is limited by the dissipative forces (viscosity) involved in moving flux through a superconductor (Ref. 4).

The net diffusion velocity of the flux lines is the difference in the probability of jumps in the opposite direction times an attempt frequency, Ω , and a jump distance, $d_{jmp} \cong d_{pin}$. Since the distance to a maximum in the potential is ξ in one direction and d_{pin} in the other (Ref. 11), the equation is somewhat messy:

$$v_{pin} = \Omega d_{pin} \left[\exp\left(\frac{\xi}{d_{pin}} x\right) - \exp(-x) \right] \exp\left(-\frac{U}{T}\right) \quad , \quad (5-6a)$$

where

$$x = \frac{d_{pin}}{\xi} \frac{J}{J_c^0} \frac{U}{T} \quad .$$

One would expect $d_{pin}/\xi > 1$, so one can ignore the backward hops except at the highest temperatures and lowest currents (e.g., $x d_{jmp}/\xi < 1$), where Eq. 5-6a takes the limiting forms:

$$v_{pin} = \Omega d_{pin} \exp\left[-\frac{U}{T} (1 - J/J_c^0)\right] \quad x > 1 \quad , \quad (5-6b)$$

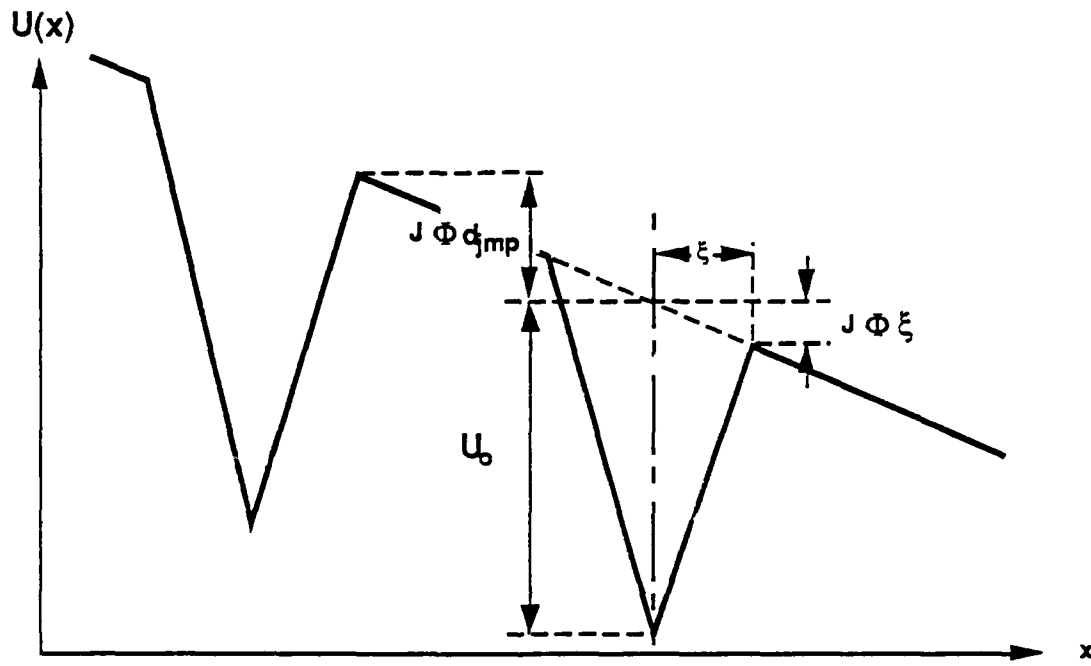


Fig. 5-1. Effect of Lorentz force $J \times B$ on the energy barrier to a unit length of flux bundle in a pinning site. The initial barrier has a height of U_0 and a width of ξ . The pinning sites are separated by a distance d_{pin} . Each bundle contains one quantum, ϕ_0 of flux.

$$v_{pin} = \Omega d_{jmp} \left(1 + \frac{d_{pin}}{\xi} \right) \frac{J}{J_c^0} \frac{U}{T} \exp \left(- \frac{U}{T} \right) \quad x < 1 \quad . \quad (5-6c)$$

Equations 5-6a through 5-6c are valid so long as the flux is strongly pinned: flux spends more time pinned than moving between pinning sites. In the weak pinning case, viscous forces limit the flux speed to

$$v_{visc} = J \Phi_0 / \eta = J \rho_n / H_{c2} \quad , \quad (5-7)$$

where η is the viscosity and ρ_n the normal resistance (Ref. 4). For intermediate strength pinning, the average flux velocity is

$$v_{flux}^{-1} = v_{pin}^{-1} + v_{visc}^{-1} \quad . \quad (5-8)$$

If we assume that v_{pin} will dominate in any region in which we are interested, we can take $v_{flux} = v_{pin}$.

The electric field, E , generated by the flux motion is just

$$E = B v_{flux} = E_0 \exp \left[- \frac{U}{T} (1 - J/J_c^0) \right] \quad x > 1 \quad , \quad (5-9a)$$

$$= E_0 \frac{J}{J_c^0} \left(1 + \frac{d_{pin}}{\xi} \right) \frac{U}{T} \exp \left(- \frac{U}{T} \right) \quad x < 1 \quad , \quad (5-9b)$$

where $E_0 = B \Omega d_{pin}$. Solving for J_c one finds

$$J_c \cong J_c^0 [1 - (T/U) \ln (E_0/E)] \quad x > 1 \quad , \quad (5-10a)$$

$$\cong J_c^0 \left(\frac{E}{E_0} \right) \left(\frac{1}{1 + \frac{d_{pin}}{\xi}} \right) \exp \left(- \frac{U}{T} \right) \quad x < 1 \quad . \quad (5-10b)$$

The size of the "critical current" J_c depends on the measurement limits for the electric field E . That is, these "super" conductors still have a finite resistance.

5.3. SUPERCONDUCTING RESISTANCE - ZERO FREQUENCY

Going back and solving the above equations for resistance, one finds that in the absence of pinning, the viscosity for flux motion for the superconductor yields a large resistance which is linear in B and T (the latter through the temperature dependence of ρ_n):

$$\rho_s = \frac{E}{J} = \rho_n \frac{B}{H_{c2}} \quad (\text{no pinning sites}) \quad (5-11)$$

$$\approx 0.01 \mu\Omega\text{-m at 1 Tesla} \quad .$$

This is no better than copper!

The presence of pinning makes things more complicated. For dc currents, the flux cannot move without hopping out of pinning sites. The hopping rate rapidly becomes very small as T decreases. One can get a feeling for this situation by looking at Eq. 5-9. For high temperatures and/or for low currents (e.g., $UJd_{pin} < \xi J_c^0 T$), Eq. 9b can be rewritten as

$$\rho \approx \rho_0 \frac{U}{T} \exp\left(-\frac{U}{T}\right), \quad (5-12)$$

where

$$\rho_0 = \frac{E_0}{J_c^0} \approx 2 \frac{\Phi_0 B}{\mu_0 H_c^2} \left(\frac{d_{pin}}{\xi}\right)^3 \Omega \quad . \quad (5-13)$$

Flux is only weakly pinned at high temperatures, so the resistance in that case is limited by the viscosity for flux flow in the superconductor

$$\rho_{\text{flux}}^{-1} = \rho_{\text{pin}}^{-1} + \rho_{\text{visc}}^{-1} \quad (5-14)$$

The resistivity, E/J , was calculated from Eq. 5-9 and plotted in Fig. 5-2 using the following parameters: $H_c = 0.82$ eV (Ref. 12) and ξ_{\perp} and $\xi_{\parallel} = 0.5$ and 2.5×10^{-9} m (Ref. 13) which give $U_0 = 0.05$ eV, $d_{\text{pin}} = 1.5 \times 10^{-8}$ m (Refs. 13 through 15), $\Omega = 10^9$ s $^{-1}$; the last was chosen to give $J_c^0 \approx 10^6 - 10^7$ A/cm 2 at 0 K. With this combination of parameters, and a field of 0.1 Tesla,

$$E_0 \approx 1.5 \text{ V/m in Eqs. 5-9 and 5-10}$$

and

$$\rho_0 \approx 7.8 \times 10^{-11} \text{ } \Omega\text{-m in Eq. 5-12}$$

All of the above parameters are temperature dependent. The Ginsberg-Landau forms are a reasonable approximation to the observed behavior (Ref. 16) and were used in the calculation of the curves in Fig. 5-2: H_c and $H_{c2} \propto (1 - t^2)$, $\xi \propto \sqrt{(1 + t^2)/(1 - t^2)}$, and $U \propto (1 + t^2)^{3/2} (1 - t^2)^{-1/2} (1 - b)^2$, where $b = H/H_{c2}$. In addition, $\rho_0(T) = \rho_0 [(1 + t^2)(1 - t^4)]^{-1/2}$. One can see that at low currents, the resistance is constant, and its value decreases rapidly with temperature. It increases dramatically as one approaches J_c .

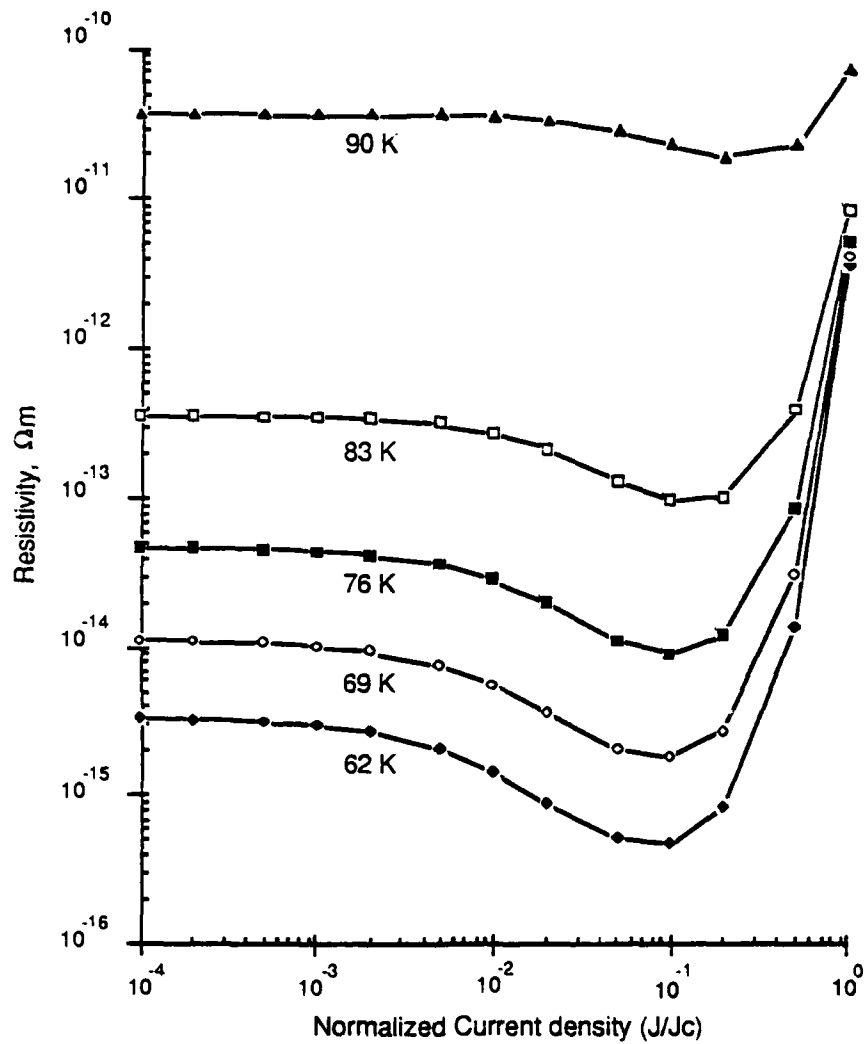


Fig. 5-2. Effective resistivity from flux creep for a high T_c superconductor with $T_c = 92$ K, $\xi_{\perp} = 2.5$ nm, $\xi_{\parallel} = 0.5$ nm, and $H_c = 0.82$ T (this gives $U_0 \cong 0.05$ eV), and $d_{pin} = 1.5$ nm. $\Omega = 10^9$ s $^{-1}$ to force J_c between 10^{10} and 10^{11} A/m 2 .

5.4. SUPERCONDUCTING RESISTANCE - HIGH FREQUENCY

For ac currents, the resistance does not disappear even for completely pinned flux. The pinning sites have a finite size, ξ , and the flux lines can move back and forth within them. There is a restoring force retarding the motion of the flux which will eventually bring them to a halt, so we assume that on the average, the flux bundles move at about half the speed they would if free. With this model, each cycle causes a resistance $Bv_{\text{visc}}/2J$ for time $2\xi/v_{\text{visc}}$. Multiplying by cycles per second, one has for the loss from this source:

$$\rho_s(\omega) = \frac{\omega \xi B}{J} \quad (5-15)$$

This only dominates at frequencies such that

$$\omega > \frac{v_{\text{visc}}}{2\xi} \quad (5-16)$$

at which point $\rho_s(\omega)$ approaches half that of unpinned flux. It increases further for higher frequencies until the flux is effectively completely unpinned; the analytic form of this increase depends on the shape of the pinning potential well.

AC currents cause resistance even at low frequencies. This is especially visible in the floppy case; the flux lines distort and move freely in between the pinned locations (Fig. 5-3). If we assumed that the Lorentz force applied to the flux bundle between pinning sites stretches it until the restoring force equals the Lorentz force. The shape (Ref. 10) of the bowed flux line is

$$y(x) = \frac{f_p}{2sC_{66}} \frac{\cosh(x/s)}{\sinh(d_{\text{pin}}^*/2s)} \quad (5-17)$$

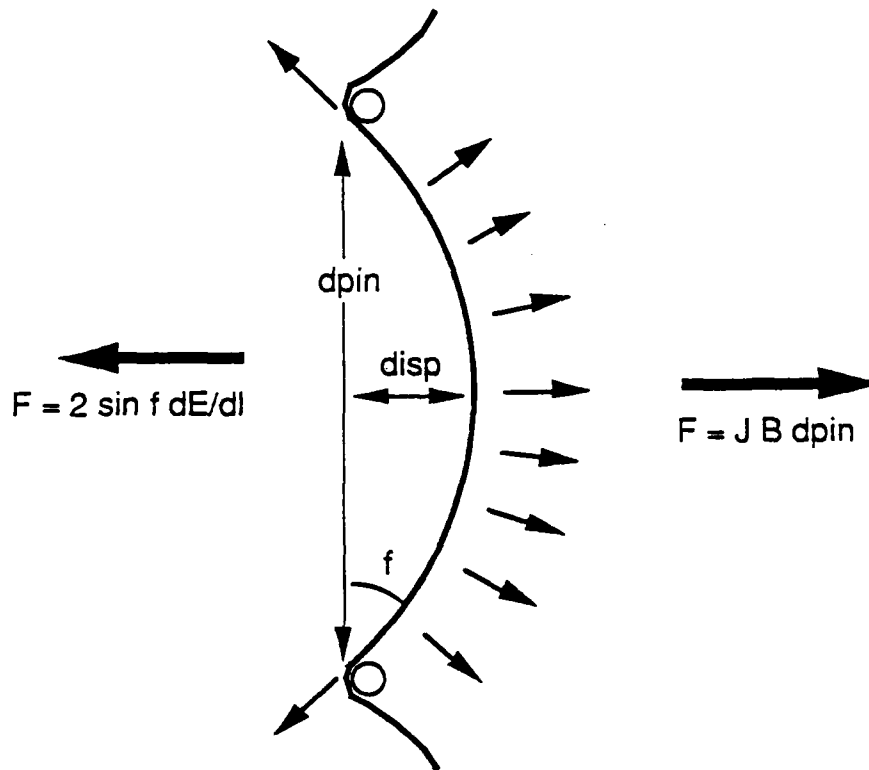


Fig. 5-3. When flux lines are floppy, the Lorentz force bows them out between pinning sites. The stretching force is normal to the curve at every point, so not counting the rigidity of the flux lines, the flux bundle is roughly bent into the arc of a circle. For small forces, the flux displacement in the center is $d_{disp} = f_p / C_{66} d_{pin}^* / 4s^2$ (Ref. 10)

The amplitude of this motion, d_{disp} , increases with the separation between sites, d_{pin} and decreases with the square of the minimum flexible length s (see Appendix A.1). This causes a motion just as described in Eqs. 5-15 and 5-16 except that only about half of the line moves to the full extent and ξ is replaced by d_{disp} . As a result, the resistance is larger and the saturation frequency is much lower.

$$\rho_s = f_{pin} \left(\frac{\omega B d_{disp}}{4s^2} \right) , \quad (5-18)$$

$$\omega > \frac{v_{visc}}{d_{disp}} . \quad (5-19)$$

The above are very crude models. A more sophisticated analysis, based on rf studies (Refs. 18 through 20) of conventional Type II superconductors have shown that flux pinning is effective below a frequency (Refs. 19 and 20)

$$\omega \approx \frac{\rho_n U_{pin}}{H_{c2}} (B\Phi_0)^{-1/2} . \quad (5-20)$$

Because the superconducting parameters are quite different for the oxide superconductors considered here, Eq. 20 may not be valid.

We suggest that it is necessary to repeat the old experiments of measuring the surface resistance of the high T_c superconductors under the external applied magnetic field. Such experiments will yield information of the nature of the flux flow and pinning in the high frequency regime and will provide a different method to determine the critical magnetic fields of the new superconductors. Measurements of the ac resistivity as a function of frequency for the samples with different pinning strength will also be useful. This type of experiment can be done in a transmission line configuration. In particular, whether the

critical frequency, ω , specified in Eqs. 5-16, 5-19, and 5-20, exists in the new superconductors, and its analytic dependence remains to be determined.

5.4.1. High Q Cavities

Finally we have derived equations needed as result of flux motion (not including ω^2 term - that is in addition) to estimate the resistivity of superconductors as function of temperature at high frequency.

Suppose one wanted to drive a 10 GHz cavity in the TE_{011} mode with a Q of 10^5 . Such a cavity would be a cylinder approximately 2 cm in radius by 3 cm long which gives $V \approx 4 \times 10^{-3} \text{ m}^3$. Suppose one could tolerate a wall loss of 1 W. Energy lost per cycle is $P \approx 10^{-10} \text{ J}$. The energy density stored in the cavity is $E \approx PQ/V \approx 3 \times 10^{-3} \text{ J/m}^3$. Average field $B = \sqrt{2E\mu_0} \approx 10^{-5} \text{ T}$ so the fields are smaller than H_{c1} in this case, and magnetic fields only penetrate a magnetic field penetration length, λ_L ; one would have to reach energy densities of MJ/m^3 for flux to penetrate as bundles.

From

$$\int H \cdot dA = \int I \cdot dS \quad , \quad (5-21)$$

one can estimate the currents needed to contain these fields. Equation 5-21 reduces in the cylindrical case to $I \text{ (A/m}^{-1}\text{)} = 5 \times 10^6 / 2\pi H(T)r(m) \approx 10 \text{ A}$ per unit length along a cylinder of radius r . The superconducting surface sets up this current in a layer whose thickness is the skin depth, $\delta \approx 0.2 \text{ } \mu\text{m}$, so the current density at the surface, $J \approx 5 \times 10^7 \text{ A/m}^2$. If power loss is $3 \times 10^{-4} \text{ W}$ for a surface area of $5 \times 10^{-3} \text{ m}^2$, then resistance can be $R = P/I^2 = 10^{-13} \text{ } \Omega\text{-m}$. One can see from Fig. 5-2 that if one only worries about the dc loss, these materials can operate up to 77 K.

Suppose the cavity had to have a Q of 10^{11} . Then the fields would be above H_{c1} and the flux would penetrate as bundles. The required current would also increase by 10^3 . The penetration depth now depends on how far the flux can penetrate in one cycle. At 10 GHz, that is far less than λ_L . For the cavity described above: $J = 5 \times 10^9$ A/m², $H_{c2} = 140$ T, and using $\rho_n \cong 1$ $\mu\Omega$ -m, one finds $\approx 4 \times 10^{11}$ s⁻¹ Eq. 5-16, implying that at a frequency of 10^{10} s⁻¹ the flux lines would move a distance of $40 \xi \approx 4 \times 10^{-8}$ m in a cycle. As a result the field penetration length is still λ_L . The required surface resistance is now $\approx 10^{-19}$ Ω -m, and these materials cannot be used above about 40 K.

At sufficiently high frequencies, the flux lines behave as if they were not pinned. For the cavity described above: $J = 5 \times 10^9$ A/m², $H_{c2} = 140$ T, and using $\rho_n \cong 1$ $\mu\Omega$ -m, one finds $\approx 4 \times 10^{11}$ s⁻¹ and 3×10^9 s⁻¹ for Eqs. 5-16 and 5-19, respectively, implying that the flux lines would be effectively pinned at 10 GHz, but that they would flop back and forth freely; the surface resistance would be nearly that of copper unless the pinning density could be raised.

5.5. SUMMARY

We have shown that flux pinning is sufficient to reduce the surface resistance of the ceramic oxide superconductors to tolerable levels only in the dc limit. At microwave frequencies, the flux lines can distort with their pinning framework and contribute an unacceptable level of loss to the superconductor.

The model developed in this paper is rather simple, and implies the same kind of ac losses in more conventional Type II superconductors. As they operate quite well at sufficiently low temperatures, it is clear that the model is incomplete and needs further investigation; at this stage it should be treated as a guide to future experiments, rather than a quantitative analysis.

TABLE 5-1
MATERIAL PARAMETERS

Maximum pinning strength and thermal activation calculated for several Type II superconductors. Underlined numbers were calculated from the others.

		Y ₁₂₃ (Ref. 12)	Pb-10% Tl (Ref. 22)	Nb-Ti (Ref. 23)	NbN (Refs. 13 and 24)	Nb ₃ Sn (Refs. 23 and 25)
(\perp , \parallel to c-axis)						
H _{c0}	(Tesla)	0.82	0.08	0.25 (Ref. 9)	<u>0.19</u>	<u>0.48</u>
H _{c10}	(Tesla)	0.5, 0.005	--	--	0.0093	0.03
H _{c20}	(Tesla)	29, 140	0.2	13	15.8	23
T _{c0}	(°K)	90	7.2	9.5	16 (Ref. 27)	18
ξ ₀	(nm)	0.5, 2.5	100	4	4.6	3
λ ₀	(nm)	810, 94	200	300	440	65
κ ₀		230, 36	1.8	70	60	22
k _B T _c	(eV)	0.007	0.0006	0.0007	0.0014	0.0016
U=H ² ξ ³	(eV)	0.02 (Ref. 5)	16	0.04	0.03	0.06
U _{exp}	(eV)	0.05 (Ref. 26)	1 to 2	--	--	--
k _B T _c /U	Maximum	0.1	0.00001	0.02	0.04	0.03
k _B T _c /U	Expt1	0.1	0.0006	-	--	--

6. REFERENCES

1. Banail, J. S., and P. K. Pohil, Synth. React. Inorg. Met. Org. Chem, 16(9), 1217 (1986).
2. Fahrenholtz, W. G., D. M. Millar, and D. A. Payne, "Preparation of $\text{YBa}_2\text{Cu}_3\text{O}_{7-x}$ from Homogeneous Metal Alkoxide Solution," Advanced Ceramic Materials, XXXX.
3. Accibal, M. A., J. W. Draxton, A. H. Gabor, W. L. Gladfelter, B. A. Hassler, and M. L. Mecartney, "Comparison of Several Cu(I) and Cu(II) Precursors for the Sol-Gel Preparation of High T_c Superconducting Metal Oxides," to be published.
- 4(a). Tinkham, M., Introduction to Superconductivity, McGraw Hill, New York (1975).
- 4(b). Tinkham, M., "Resistive Transition of High-Temperature Superconductors," Phys. Rev. Lett., 61, 1658 (1988).
5. Yeshurun, Y., and A. P. Malozemoff, "Giant Flux Creep and Irreversibility in an Y-Ba-Cu-O Crystal: An Alternative to the Superconducting Glass Model," Phys. Rev. Lett., 21, 2022 (1988).
6. Anderson, P. W., Phys. Rev. Lett., 9, 309 (1962).
7. Kim, Y. B., Rev. Mod. Phys., 36, 39 (1964).
8. Campbell, A. M., and J. E. Evetts, "Flux Vortices and Transport Currents in Type II Superconductors," Phys. Rev., 181, 682 (1972).
9. Malozemoff, A. P., T. K. Worthington, Y. Yeshurun, F. Holtzberg, and P. H. Kes, "Frequency Dependence of the AC Susceptibility in an YBaCuO Crystal: A Reinterpretation of H_{c2} ," Submitted to Phys. Rev., B (1988).
10. Kramer, E. J., "Scaling Laws for Flux Pinning in Hard Superconductors," J. Appl. Phys., 44, 1360 (1973).

11. Sun, J. Z., K. Char, M. R. Hahn, T. H. Geballe, and A. Kapitulnik, "Magnetic Flux Motion and its Influence on Transport Properties of the High T_c Oxide Superconductors," App. Phys. Lett., 54, 663 (1989).
12. Worthington, T. K., W. J. Gallagher, and T. R. Dinger, "Anisotropic Nature of High-Temperature Superconductivity in Single Crystal $Y_1Ba_2Cu_3O_{7-x}$," Phys. Rev. Lett., 59, 1160 (1987).
- 13(a). Kes, P. H., "Irreversible Magnetic Properties of High T_c Superconductors," Physica, C153-155, 1121 (1988).
- 13(b). Kes, P. H., J. Aarts, J. van den Berg, C. J. van der Beek, and J. A. Mydosh, "Thermally Assisted Flux Flow at Small Driving Forces," to be published in Superconductor Science and Technology (1988).
- 14.
15. Dolan, G. J., G. V. Chandrashekar, T. R. Dinger, C. Feild, and F. Holtzberg, "Vortex Structure in $YBa_2Cu_3O_7$ and Evidence for Intrinsic Pinning," Phys. Rev. Lett., 62, 827; Pinning Structure on Scale <100 nm (1989).
16. Watanabe, K., H. Yamane, H. Kurosawa, T. Hirai, N. Kobayashi, H. Iwasaki, and K. Noto, "Critical Currents at 77.3 K Under Magnetic Fields up to 27 T for an Y-Ba-Cu-O Film Prepared by Chemical Vapor Deposition," Appl. Phys. Lett., 54, 575; Observed Maximum Pinning Strength at 9 T When $B_{c2} \approx 35$ T $\rightarrow a_0 \approx 0.015$ μ m.
17. De Vries, J. W. C., G. M. Stollman, and M. A. M. Gijs, "Analysis of the Critical Current Density in High- T_c Superconducting Films," to be published in Physica C (1989).
18. Cardona, M., G. Fischer, and B. Rosenblum, Phys. Rev. Lett., 12, 101 (1964).
19. Rosenblum, B., M. Cardona, and G. Fischer, RCA Review, 25, 491 (1964).
20. Gittleman, J. I., and B. Rosenblum, Phys. Rev. Lett., 16, 734 (1966).
21. Gallagher, W. J., T. K. Worthington, T. R. Dinger, F. Holtzberg, D. L. Kaiser, and R. L. Sandstrom, Physica, 14B, 228, Amsterdam (1987).

22. Beaseley, M. R., R. Labusch, and W. W. Webb, "Flux Creep in Type-II Superconductors," Phys. Rev., 181, 682 (1969).
23. Anderson, H. L., Ed., Physics Vade Mecum, AIP, New York (1981).
24. Roberts, B. W., J. of Phys. and Chem. Ref. Data, 5, 581 (1976).
25. Roberts, B. W., Properties of Selected Superconductor Materials: 1978 Supplements, NBS Techn. Note 983 (October 1978).
26. Dew-Hughes, D., "Model for Flux Creep in High T_c Superconductors," Cryogenics, 28, 674 (1988).
27. Kittel, C., Introduction to Solid State Physics, 3rd Ed., John Wiley & Sons, New York (1968).

APPENDIX A

A.1. MINIMUM FLEXIBLE LENGTH OF FLUX LINE, s [Derived from expressions Kramer (Ref. 10)]

We define s as the distance between pinning pins such that the maximum flexing of the center of a flux line, $d_{disp} = \xi$. If $d_{disp} > \xi$, then the line could hop from a pinning site in the center of the line without hopping from either of its neighbors. The maximum force one can exert on the line is U_{pin}/ξ . The shape of the flux line is given by Kramer (Ref. 10) - in our notation, as

$$y(x) = \frac{U_{pin}}{2s \xi C_{66}} \frac{\cosh(x/2s)}{\sinh(d_{pin}/2s)}, \quad (A-1)$$

where the shear modulus C_{66} (n/m^2) = $1.5 \times 10^5 H_c^2(T) (1-h)^2$, $h = H/H_{c2}$, $d_{pin} = s$, and $U_{pin} = 1/2 \mu_0 H_c^2 \xi^3 (1-h)^2$. This displacement of the center relative to the ends is just

$$y(0) - y(1/2) = \frac{\mu_0 \xi^2}{6 \times 10^5 s} \frac{\cosh(1/2) - 1}{\sinh(1/2)}. \quad (A-2)$$

Setting $y(0) - y(1/2) = \xi$ and solving for s one finds:

$$s = 3.2 \xi. \quad (A-3)$$

A.2. DISTANCE BETWEEN EFFECTIVE PINNING CENTERS, d_{pin}^*

The only effective pinning sites lie within ξ of the maximum flex distance of the flux line. A flux line with pins separated by $2d_{pin}^*$ probes a volume $\xi d_{disp} d_{pin}^*$. The product of the volume probed and the density of pinning sites is the probability of finding a pinning center

between the two original pinning sites. If the density of pinning centers is $1/d_{pin}^3$, then one finds

$$d_{pin}^* = d_{pin}^3 / \xi d_{disp} \quad . \quad (A-4)$$

One finds from Eq. A-1

$$d_{disp} = \frac{\mu_0 \xi^2}{6 \times 10^5 s} \frac{\cosh (d_{pin}^*/2s) - 1}{\sinh (d_{pin}^*/2s)} \quad . \quad (A-5)$$

Since $d_{pin}^*/2s < 1/2$, Eq. A-5 can be simplified to

$$d_{disp} = \frac{\mu_0 \xi^2 d_{pin}^*}{1.2 \times 10^6 s^2} \quad , \quad (A-6)$$

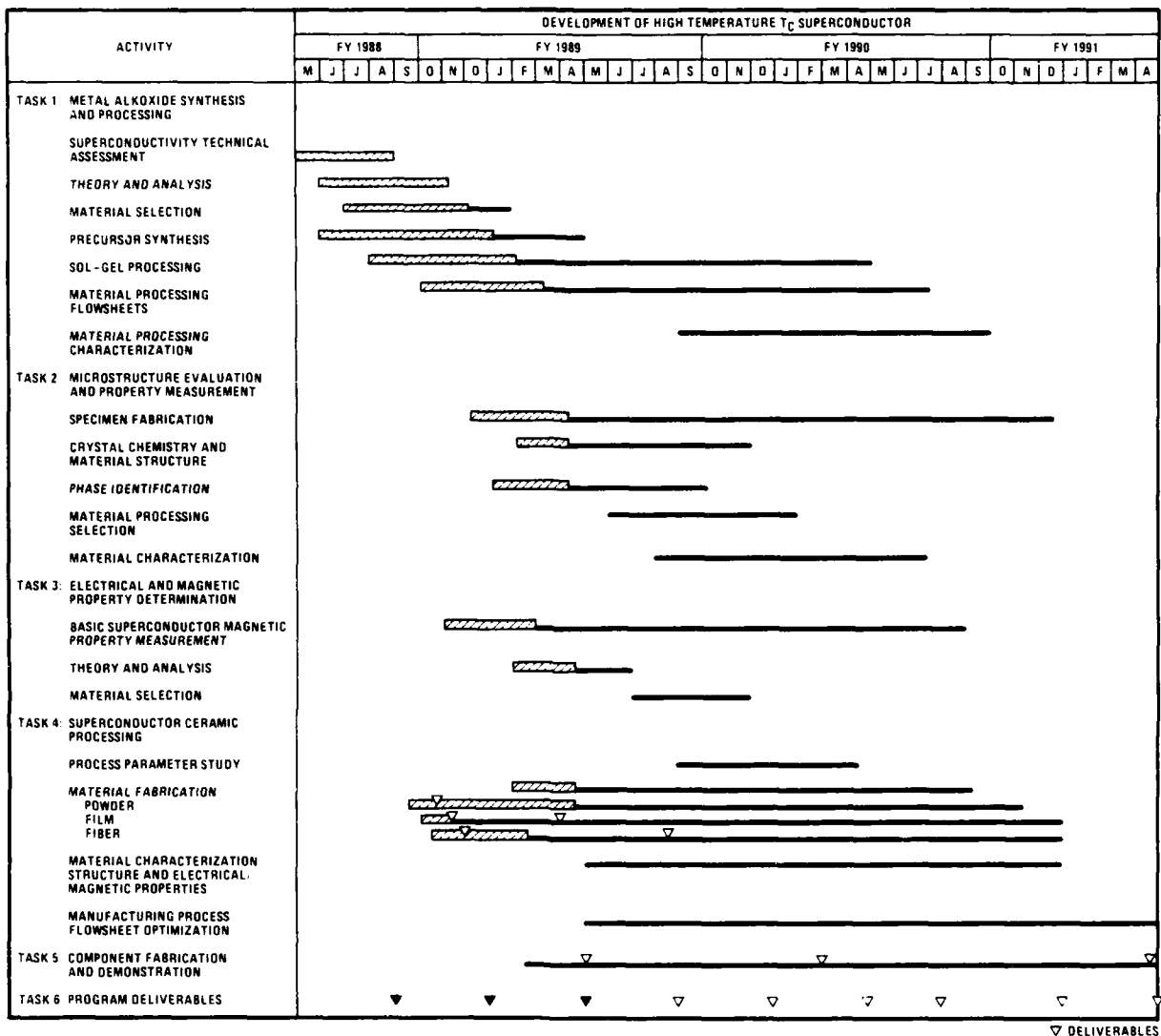
so

$$d_{pin}^* = 0.4 s \left(\frac{d_{pin}}{\xi} \right)^{3/2} \quad , \quad (A-7)$$

and

$$n_p = s/d_{pin}^* = 2.5 \left(\frac{\xi}{d_{pin}} \right)^{3/2} \quad . \quad (A-8)$$

One can see from Eq. A-8 that $n_p \cong 1$ unless the density of pinning sites is extremely high.



▽ DELIVERABLES